ADVANCED ACTIVE OUTPUT FILTER FOR LOW ACOUSTIC NOISE ADJUSTABLE SPEED DRIVE (ASD) SYSTEM

A Thesis

by

WEIRAN DAI

Submitted to the Office of Graduate and Professional Studies of
Texas A&M University
in partial fulfillment of the requirements for the degree of

MASTER OF SCIENCE

Chair of Committee,	Prasad Enjeti
Committee Members,	Hamid A. Toliyat
	Peng Li
	Wei Zhan
Head of Department,	Miroslav M. Begovic

August 2016

Major Subject: Electrical Engineering

ABSTRACT

In recent years, the acoustic noise emitted by electric motors has become an important topic. Many manufactures of adjustable speed drive (ASD) make effort to reduce the acoustic noise from electric motors. And low acoustic noise motors can be widely applied in the next generation transport system such as electric shipboard, more electric aircraft and electric vehicle. Traditionally, LC passive filters can be employed to decrease acoustic noise by mitigating the pulse-width modulation (PWM) generated voltage/current harmonics in the audible noise range. However, the bulky passive filters contribute to additional volume and cannot effectively eliminate harmonics at low switching frequency.

In this thesis, an active output filter (AOF) is proposed to replace passive filters in ASD. The proposed AOF is implemented by the harmonic injection strategy, which can compensate voltage/current harmonics at the arbitrary frequency. Therefore, the acoustic noise, which partly generates from PWM inverter-fed ASD, is decreased dramatically. In addition, AOF offers a substantial volume reduction and high power efficiency by using wide-band gap devices. In this thesis, two different motor drive structures including single-phase ASD, three-phase ASD are investigated to verify the advantages of the proposed AOF.

ACKNOWLEDGEMENTS

First, I would like to express my appreciation to my advisor and committee chair, Dr. Prasad Enjeti, for his patience, motivation and academic guidance. During two year graduate study, Dr. Enjeti always encourages me to explore new technology.

I also would like to thank my committee members, Dr. Toliyat, Dr. Zhan and Dr. Li. I appreciate your time and support.

I have a great experience in Power Quality Lab at Texas A&M University. In our lab, I get much help from Yong Zhou, Taeyong Kang, Fahad Alhuwaishel, Ahmed Salah Morsy, Michael T. Daniel, Bahaa Hafez, Jorge Ramos, Jose Sandoval, Harish Krishnamoorthy, Somasundaram Essakiappan and Angela Clark. A special thanks to visiting professor Dr. Dongyuan Qiu, who gives detailed guidance for my research.

I also thank my friends at Texas A&M University, Zichao Xie, Chang Zhong, Yixuan Chai, Tian Lan, Shunlong Xiao, Yongqi Li, Xiao Li, Zhan Wang, Haiyu Zhang, and Hezi Zhu. Hope everyone can enjoy the work and life.

Finally, I thank my parents, Bing Dai and Sihong Ding, for always supporting and encouraging me over 20 years.

TABLE OF CONTENTS

Page

LIST OF FIGURES

Page

LIST OF TABLES

Page

1. INTRODUCTION

1.1 Background

Electric energy becomes the major source of energy around the word nowadays. The estimated electric production of the world increases rapidly every year shown in Fig. 1-1. And about 46% of the electric energy is consumed by different motor drives [1]. It is obvious that optimization design of motor drive is very significant for electric consumption reduction.

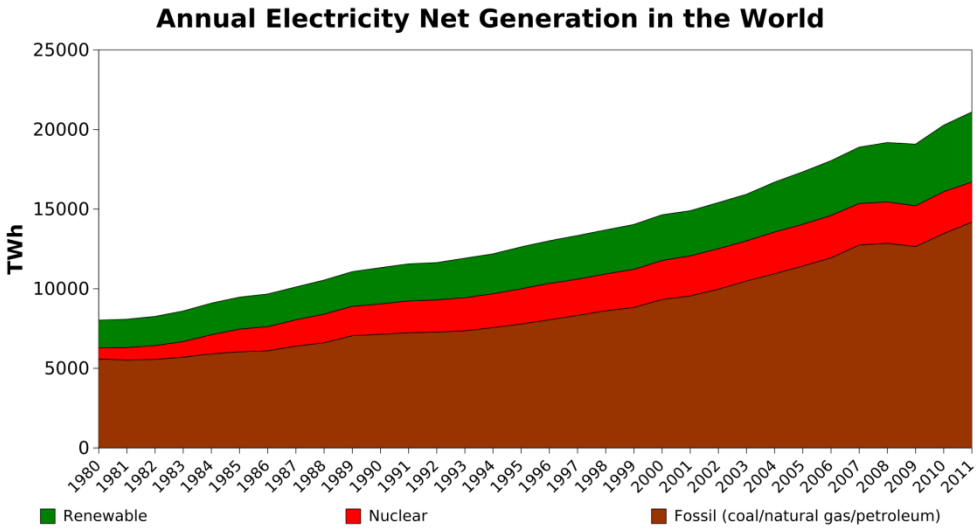

Fig. 1-1. Annual electric production in the world [2].

An electric motor is a system that converters electrical energy into mechanical energy. Motors power rating is from several hundred watts to several hundred kilowatts. Electric motors are always classified according to power source type and operation theory as shown in Fig. 1-2. Generally speaking, DC motor is applied for low power area and its power efficiency is not very high. On the other hand, AC motor is suitable for

high power application and provides high power efficiency. AC motor includes synchronous motor and induction motor. Induction motor is more cost-effective than synchronous motor and hence, it is widely applied in the electric vehicle, fan, pump and so on in the industrial and residential areas.

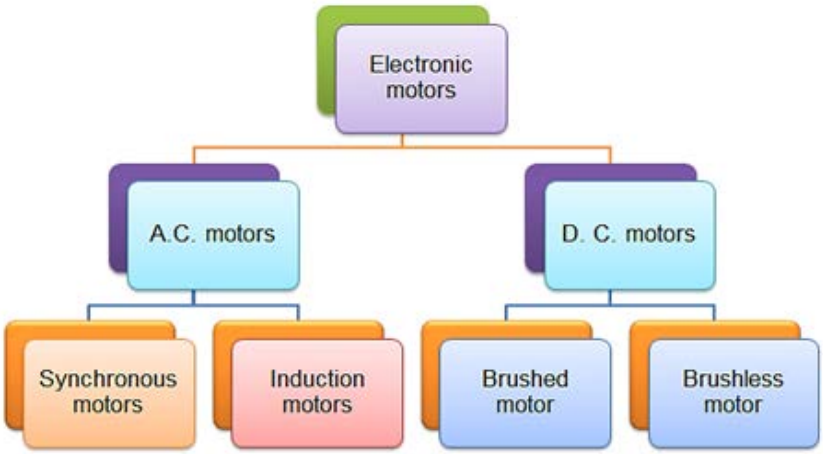

Fig. 1-2. Electric motor categories [3].

In order to control the induction motor operation, some induction motor drives are developed in recent years. Constant speed drive (CSD) and adjustable speed drive (ASD) are both popular drive system for induction motor application. For CSD, the operation frequency is fixed and hence the motor speed cannot be changed. As for ASD, the motor speed can be adjusted by controlling the operation frequency, which can satisfy modern induction motor requirement. In addition, ASD system can achieve higher power efficiency and improve reliability and robust dynamic performance [4]. When a motor is run at half speed, it consumes significantly less energy than it does at full speed.

1.1.1 Overview of Adjustable Speed Drive

A typical motor drive system is composed of ASD, induction motor, controller and measurement unit, which is shown in Fig. 1-3.

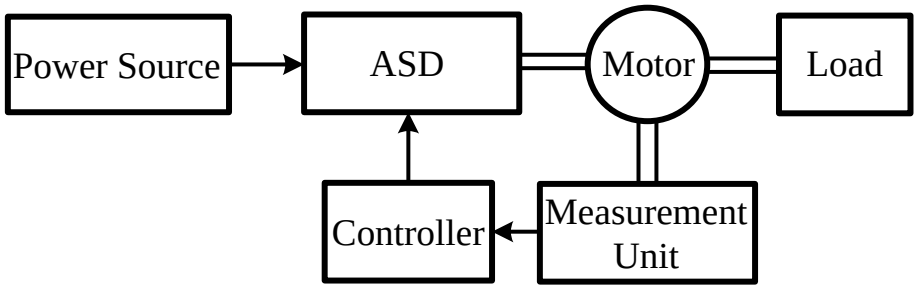

Fig. 1-3. Motor drive system using ASD

A detailed ASD shown in Fig. 1-4 includes several power electronics blocks as follows:

- Front end three-phase rectifier
- DC link filter
- Back end 3-phase inverter
- Passive filter

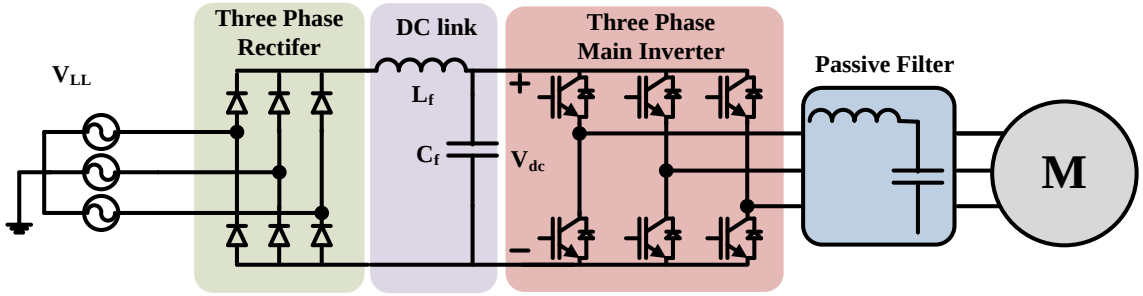

Fig. 1-4. Traditional three-phase ASD system.

The frond end three-phase rectifier converts utility AC voltage to DC voltage. After DC link filter including the inductor and electrolytic capacitor, the DC link voltage can be derived as:

$$V_{dc} = \sqrt{2}\frac{3}{\pi}V_{L-L} \tag{1-1}$$

where V_{L-L} represents line-line RMS voltage.

The 3-phase PWM inverter transfers DC voltage to 3 phase AC voltage. The output AC voltage amplitude and frequency can be controlled by the inverter. Output passive filter is employed to reduce the voltage/current harmonics. The ideal AC voltage amplitude can be determined as [5]:

$$V_{AN,L-L} = \sqrt{3}\frac{m_a}{2}V_{dc} \tag{1-2}$$

where m_a denotes the modulation index.

Combining (1-1) and (1-2), the output AC voltage amplitude can be expressed as the input line voltage.

$$V_{AN,L-L} = \frac{3\sqrt{6}m_a}{2}V_{L-L} \tag{1-3}$$

1.1.2 Need for Low Acoustic Noise in ASD

The environmental problem related to acoustic noise produced by electric motor has been an important topic recently. The sound was defined as the wave motion by Helmholtz and others. A sound wave in air comes from variations in pressure above and below undisturbed air. There are two widely used measurements to represent sound

level: sound intensity and sound pressure [6]. Sound intensity is defined as the sound power per unit area. The standard threshold for sound intensity is:

$$I_o = 10^{-12} Wm^{-2} \tag{1-4}$$

This value corresponds to 0dB. Therefore, the real sound intensity can be calculated relative to (1-3).

$$I(dB) = 10\log_{10}(\frac{I}{I_o}) \tag{1-5}$$

In the practical world, the surrounding environment is vital in shaping the sound wave during the transmission. Another measurement sound pressure level (SPL) is popular due to the consideration of the surrounding factors. Sound pressure is defined as the pressure vibration amount and the standard threshold value is:

$$SPL_o = 2 \times 10^{-5} Nm^{-2} \tag{1-6}$$

Similar with sound intensity, SPL is also described in dB and determined as following. Generally, SPL is used to represent how loud the sound is.

$$SPL(dB) = 10\log_{10}(\frac{SPL^2}{SPL_o^2}) \tag{1-7}$$

Table 1-1 shows the SPL level restriction of common sounds. It is clear heave industry such as aircraft, shipboard, submarine exist the severe acoustic noise issue. In these applications, acoustic noise is mainly from electric motors. Therefore, designing the low acoustic noise ASD system is very attractive. On the other hand, low acoustic noise ASD is beneficial to avoid the sonar tracking in shipboard and submarine applications.

Table 1-1. Sound pressure level of common sounds

Example of sound	SPL (dB)
Threshold of pain	130
Vehicle	80
Open public area	40
Office	35
Aircraft	120
Shipboard	100
Submarine	130

1.1.3 Acoustic Noise Sources in Electric Motor

In order to reduce the acoustic noise in electric motor, it is necessary to figure out the sources of acoustic noise as illustrated in Fig. 1-5. Normally, the sources are classified into three categories:

- Mechanics
- Aerodynamic
- Electromagnetic

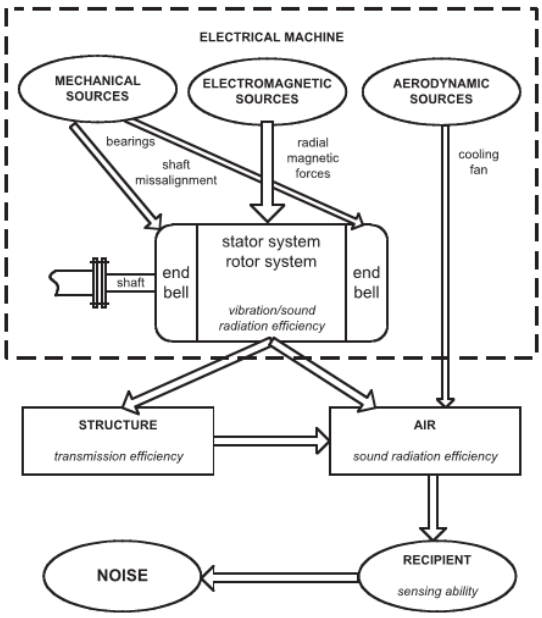

Fig. 1-5. Noise generation in typical electrical machines.

This chapter will review these sources in ASD system with induction motor. First, the relationship with vibration and noise is introduced. In the induction motor, a surface vibrates or moves to induce the disturbance. The movement of these surfaces is defined as the vibration. The propagated sound by these surfaces is defined as the acoustic noise [7].

(1) Mechanical Origins

Some usual mechanical sources include bearings, rotor unbalance, concentricity and resonance. Bearings are connection between rotor and stator, which allow the displacement of rotor and stator. The bearing effect becomes more significant with the speed incensement. Sleeve bearings produce the low magnitude of acoustic noise, while rolling ball bearings induce more acoustic noise, especially for low power and small induction motor [8]. Main factors affect the bearing vibration are following: (1) geometry discrepancies between rolling elements; (2) mechanical resonance frequency of the ring; (3) operation temperature; (4) alignment of the shaft.

Rotor unbalance is another cause of the mechanical vibrations. If the rotor winding distribution is not uniform and there is a mismatch between the geometric center of the body and gravity center, then the dynamic force is induced to excite the vibration during the rotation [9]. Unbalance rotor results from asymmetry structure, material uniformities and so on.

Concentricity of the rotor and stator is important to maintain the uniform permeance of the airgap. For induction motor, the radial force is smaller than other

motor types, and hence, it is slightly more tolerant to concentricity misalignment.

Generally, induction motor has several natural resonant frequencies. Resonance will occur if the excitation magnetic force frequency matches the natural frequency or multiple of it, which results in huge vibration at the resonant frequency [10].

(2) Aerodynamic Origins

Aerodynamic source results from air disturbance with the motor rather than motor vibration. The first part of aerodynamic related noise is the fluctuation of air pressure due to rotor rotation, which depends on rotating speed. The second part is from periodic fluctuation of air due to resonance excitation, which is independent of rotating speed.

(3) Electromagnetic Origins

For induction motor, it is necessary to excite the magnetic flux to provide the mechanical rotation. No matter which magnetic flux excitation method is used, this will induce the vibration in the induction motor, which is mainly located in the air-gap. The electromagnetic noise depends on two types of harmonics [11]:

- Space harmonic: it is related to discretization of stator and rotor winding. These harmonic is the function of the stator and rotor slot number and distribution. Space harmonic exists even with the pure sinusoidal power supply.
- Time harmonic: it appears in the inverter-fed ASD. For PWM mode ASD, this harmonic mainly results from the current harmonic distributed in multiples of switching frequency sidebands.

1.2 Literature Review

1.2.1 Analysis and Prediction of Acoustic Noise

Beginning from the 20th century, researchers has contributed to investigating the acousice noise characterazation in the electric motor. In 1950s, Liwschitz Garik proposed the calculation methodology for air gap radial magnetic force in the induction motor. In 1965, H. Jordan put forward the geometric similarity theory of the motor design is not applicable for acousitc noise analysis. Instead of it, spherical radistor method is proposed to calculate the acousitc noise for induction motor [12]. In 1981, R. S. Girgis analyzed the natural frequency and pointed out the resonance has the huge effect on acoustic noise [13]. In 1989, the acousic noise is predicted based on vibration speed on the motor surface by Z. Q. Zhu[14].

From 1970s, with the cimputer technology development, finite element analysis (FEA) becomes a popular methodology to analyze the acoustic noise quickly. T. Kobayashi compared the acoustic noise for different slot number of the induction motor based FEA model [15].

Recently, more and more acoustic noise analysis and prediction is based on experimental results. In [16], A. C. Binojkumar presented the carrier frequency and fundamental frequency effect on the acousitc noise in PWM inverter-fed ASD as shown in Fig. 1-6. It shows the overall noise level increases dramatically when the resonance occurs.

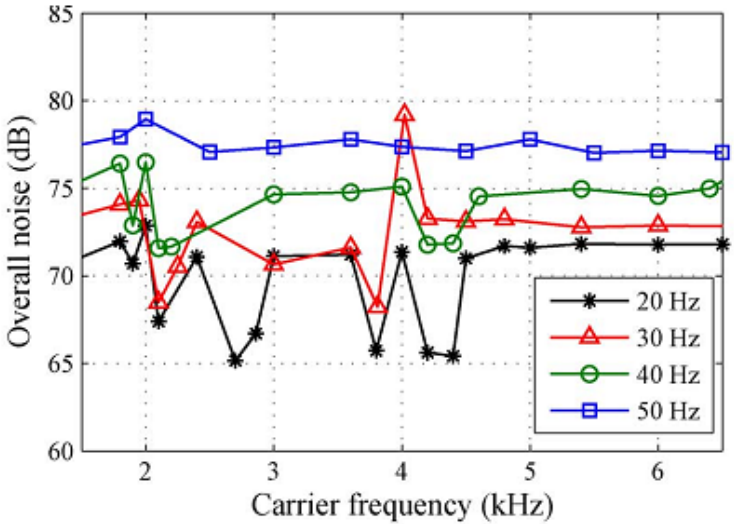

Fig. 1-6. Overall noise emmitted by 8-hp motor at various carrier and fundamental frequency [16].

Another emerging method is the acoustic noise imaging technique [17]. In this method, a 3D FEA has been modeled to calculate the acoustic noise on the motor surface as shown in Fig. 1-7.

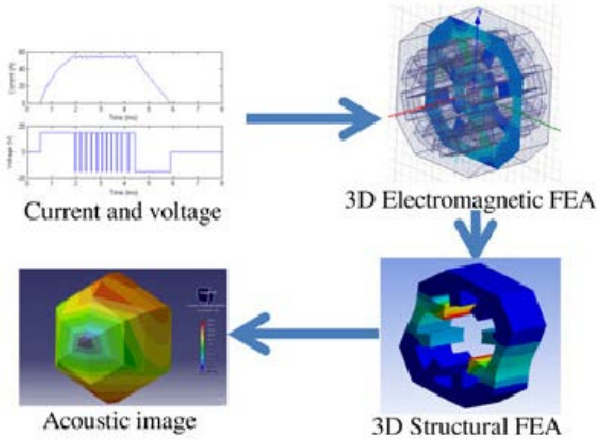

Fig. 1-7. 3D acoustic imaging for electric motor [17].

1.2.2 Methods to Reduce The Acousitc Noise

Basically, the asouctic noise can be reduced by optimizing motor design and ASD design. For the motor design, S.R. Huang found oblique slot structure can reduce the acoustic noise effecttively [18]. J. L. Besnerais proposed the stator shape design rule to avoid the resonance between mechanical structure and PWM generated magnetic force [19]. In addition, dynamic rotor balancing methodology which figures out the rotor unbalance issue can reduce the acoustic noise from mechanic sources [20].

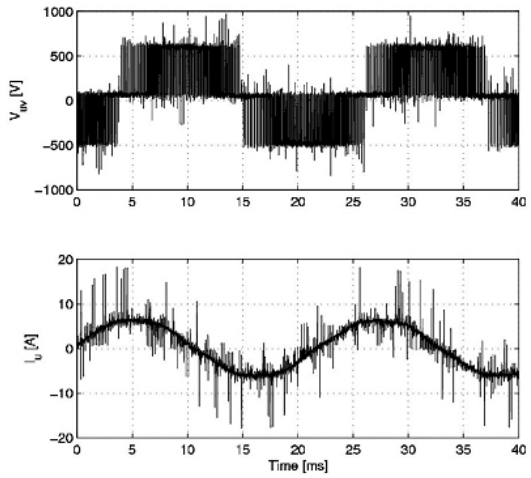

(a)

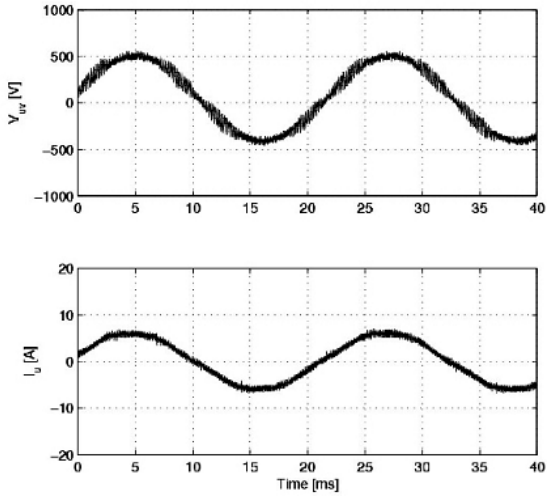

(b)

Fig. 1-8. (a) ASD output voltage and current without passive filter. (b) voltage and current with filter [21].

PWM mode inverter is widely used in the ASD system. The inverter controls the voltage to the motor by sending a series of high-voltage pulses to the motor as shown in Fig. 1-8(a), which may cause the resonance with the motor. Many manufactures such as Danfoss, Belden and Schneider take advantage of passive LC filter to generate the pure sine wave voltage shown in Fig. 1-8(b). Since the distortion is eliminated, the related acoustic noise is depressed. However, passive filter still has some drawbacks:

- A voltage drop is introduced between ASD and motor.
- Increased cost and size.
- Because gain is not low enough in low switching frequency as shown in Fig. 1-9, cannot mitigate the acoustic noise in low switching frequency.

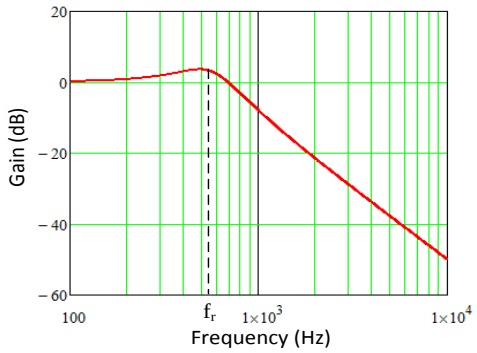

Fig. 1-9. Transfer function of a typical damped LC filter employed in the 2.1 kHz switching frequency induction motor.

Another traditional method is to apply high switching frequency over audible frequency range. For the human beings, the audible frequency range is about 20 to 20k Hz. However, some disadvantages in this strategy:

- Risk of motor insulation damage.
- High thermal stress.
- VA rating restriction.

Recently, random PWM (RPWM) technology is proposed to mitigate the acoustic noise, RPWM is a low cost and digital control based strategy. In this strategy, the carrier frequency is modulated using the pseudorandom code, which can break up the regular tonal spectrum and spread harmonics over a wide range. Some popular RPWM methods are reviewed here. One is random pulse position modulation [22]. This technique is based on adjusting the duration of the zero vector or three pulse related positions in one switch period. Another methodology is random switching frequency modulation [23]. This modulation can be achieved through varying the carrier wave slope. The third strategy is the hybrid RPWM modulation [24]. This modulation is produced through randomly composing two opposite phase triangular carries with the same frequency. Fig. 1-10 shows the detailed waveforms of the hybrid RPWM. No matter which RPWM modulation is used, the PWM generated harmonics still exist in the audible frequency range, and hence, the overall emitted noise is not reduced dramatically.

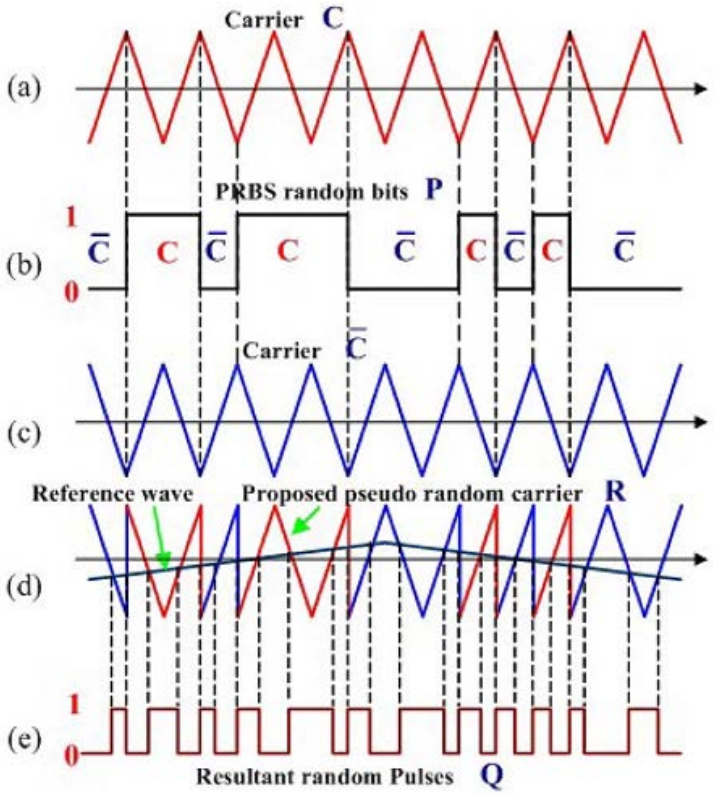

Fig. 1-10. Hybrid RPWM modulation [24].

1.3 Research Objective

In this thesis, an active output filter (AOF) is introduced as a retrofit replacement for the bulky LC filter to further reduce acoustic noise in ASD system installed in electric vehicle, shipboard and submarine. Contrary to the conventional series active power filter acting as the variable impedance [25], the proposed AOF is implemented by H-bridge switch using the harmonic injection methodology. Due to this characteristic, stator voltage/current harmonics in the audible frequency range can be completely eliminated in theory, which is beneficial to lower the acoustic noise of the induction motor dramatically.

Second, the proposed AOF operates at high switching frequency, which offers the high power density. In this thesis, the detailed volume comparison shows AOF volume is much smaller than traditional passive filter.

Third, the proposed AOF can be dynamically adjusted for different operation conditions. For example, when the grid sags, the DC link voltage of AOF is reduced to generate the appropriate harmonic injection for this scenario.

Fourth, compared to the intermediate DC voltage of ASD (after rectifier), the DC link voltage of AOF is much lower in three phase IM application, which is beneficial to decrease VA rating of AOF switches.

Last, the ringing voltage overshoot is a severe issue in the long cable induction motor. By using the AOF, the stator current and voltage is almost pure sinusoidal waveforms. Therefore, the voltage peaking is mitigated during the switch transition.

1.4 Thesis Outline

This thesis is organized in the following manner. In section 1, the brief introduction about AOF is provided. This section talks about the need for low acoustic noise ASD system and briefly analyzing the main acoustic noise sources in ASD system. Then, the previous work related to acoustic noise analysis in ASD and acoustic noise reduction methods is reviewed. The drawbacks of the existing solutions are discussed and the research objective is presented.

In Section 2, the electromagnetic noise is analyzed to demonstrate passive filter cannot mitigate the electromagnetic noise in low frequency range. However, by using AOF, the electromagnetic noise in the arbitrary frequency can be eliminated. The

proposed AOF concept is also detailed in section 2. The topology and control strategy is discussed. Small signal model of AOF is built for closed-loop control design.

Section 3 presents the single-phase ASD with AOF. The volume comparison between passive filter and AOF is shown in this Section. Simulation and experimental results illustrate the advantage of AOF for reducing the acoustic noise.

The AOF is applied in the three-phase ASD in Section 4. The step by step parameter design is detailed in design example. By using AOF, the power density is much higher than the passive filter. Simulation and experimental results show the acoustic noise is effectively suppressed in three phase ASD with AOF.

Section 5 provides the conclusion of the work and future work.

2. PROPOSED ACTIVE OUTPUT FILTER

2.1 Preliminary Electromagnetic Noise Analysis

As mentioned in Section 1, the main acoustic noise sources include aerodynamic noise, mechanical noise and electromagnetic noise. For PWM inverter-fed ASD system, the electromagnetic noise is the dominate part of the overall acoustic noise. If PWM harmonics frequency is close to the mechanical natural frequency, the resonance will occur to induce the huge electromagnetic noise. Therefore, exploring the electromagnetic noise characterizations is necessary to find the low acoustic noise solution in ASD system.

Typically, the electromagnetic noise can be determined from the radial vibration force density [26].

$$v(\alpha,t) = B^2(\alpha,t)/(2\mu_0) \tag{2-1}$$

where $B(\alpha,t)$ is the air-gap flux density, α is the angular position and t is the time. μ_0 is the vacuum permeability, $4\pi\times10^{-7}$ H/m.

Generally, flux density is the product of air gap MMF and the permeance.

$$B(\alpha,t) = F(\alpha,t)\lambda(\alpha,t) \tag{2-2}$$

In (2-2), the peameance can be expressed as below [27].

$$\lambda = \Lambda_0 + \sum\lambda_1 + \sum\lambda_2 \tag{2-3}$$

where the three terms denote permeance related to air-gap length, stator slotting and rotor slotting, respectively.

Due to the dominant effect of the first term in (2-3), the slotting permeance can be neglected. Therefore, in the PWM mode inverter-fed induction motor, air-gap flux density can be achieved as

$$B(\alpha,t)=\Lambda_0[F_1(\alpha,t)+\sum_{k=1}^{\infty}F_k(\alpha,t)+\sum_{\upsilon}^{\infty}\sum_{\mu}^{\infty}(F_\upsilon(\alpha,t)+F_\mu(\alpha,t)+F_{\upsilon\mu}(\alpha,t))+\sum_{k}^{\infty}\sum_{\upsilon}^{\infty}F_{k\upsilon}(\alpha,t)+\sum_{k}^{\infty}\sum_{\mu}^{\infty}F_{k\mu}(\alpha,t)] \tag{2-4}$$

where k is the stator current harmonic order. μ and ν denote the slot harmonic order of stator and rotor, respectively.

In (2-4), the first term is the fundamental flux density, which is always generated from fundamental frequency current. The second term denotes the flux density harmonics due to PWM generated current harmonics, which can be called pure PWM flux density harmonics. The third term represents flux density harmonics from the space harmonics in stator, rotor and intersection of stator and rotor. These harmonics are related to the slot configuration and number in the stator and rotor. The fourth and fifth term denote flux density harmonics produced by intersection of current harmonics and space harmonics.

The amplitude of the pure PWM flux density harmonics is much higher than other types of flux density harmonics, especially for no load or light load operation [28]. Moreover, the dominant portion of pure PWM flux density harmonics are normally generated by the interaction between the fundamental air-gap field and the first order field harmonic due to current harmonics, and the frequencies are given by

$$f=\left|\pm f_k-f_0\right| \tag{2-5}$$

$$f_k = n_1 f_{inv} \pm n_2 f_0 \quad (2\text{-}6)$$

where f_0 denotes the fundamental frequency of stator current/voltage. f_k and f_{inv} are the current harmonic frequency and inverter switching frequency, respectively. n_1 and n_2 are both integers, where, if n_1 is an even number, n_2 will be an odd number and vice versa.

According to (2-4) - (2-6), magnetic noise is mainly distributed in the fundamental frequency and switching frequency sideband. For ASD system with LC filter, it can be predicted that magnetic noise peaking will appear in fundamental frequency and low order switching frequency sideband. However, due to the harmonics compensation at the whole frequency spectra, magnetic noise spike will be only in the areas of fundamental frequency in the induction motor with AOF.

2.2 Topology

The proposed AOF employs the DC voltage in the capacitor and transfers it to the AC harmonics which inject into the stator voltage and current. Due to the opposite phase harmonics injection, the PWM generated stator voltage/current harmonics are cancelled. The proposed AOF has the following advantages:

- ASD with the proposed AOF achieves higher power density.
- AOF only includes a very small inductor which can carry large current without magnetic saturation.
- The ringing voltage overshoot is eliminated at the motor terminals.
- Acoustic noise of induction motor is lower than the conventional ASD with the passive filter.
- Low DC link voltage of AOF decreases VA rating of switches.

The power stage of the proposed AOF is shown in Fig. 2-1. The proposed AOF block consists of small high frequency filter L_a, C_a, a DC-link capacitor C_d and the GaN FET based H-bridge inverter operating at high switching frequency (48 kHz). GaN FET is the emerging wide-gap-band device which offers high switching frequency, low on-state resistance and no reverse recovery current. Due to the characteristic of GaN FET, the AOF can achieve high power density and low power loss. The DC link capacitor resembles a DC voltage source for voltage harmonics injection. The AOF output V_{aof} described by (2-7) provides the proper voltage injection to maintain the pure sinusoidal voltage for the load.

$$V_{aof} = V_{inv} - V_z = V_{inv} - V_{dc} M \cos(w_0 t) \tag{2-7}$$

where M and V_{dc} represent modulation index and DC link voltage of main inverter, respectively. V_{inv} is the inverter output voltage including PWM harmonics. The value of V_{inv} is determined by the specific modulation strategy. Section 3 and 4 will introduce the single-phase inverter and three-phase inverter PWM modulation strategies, respectively.

Due to the constant voltage in C_d, the switching function for H-bridge can derived from (2-7).

$$S_{aof} = \frac{V_{inv} - V_{dc} M \cos(w_0 t)}{V_{cap}} \tag{2-8}$$

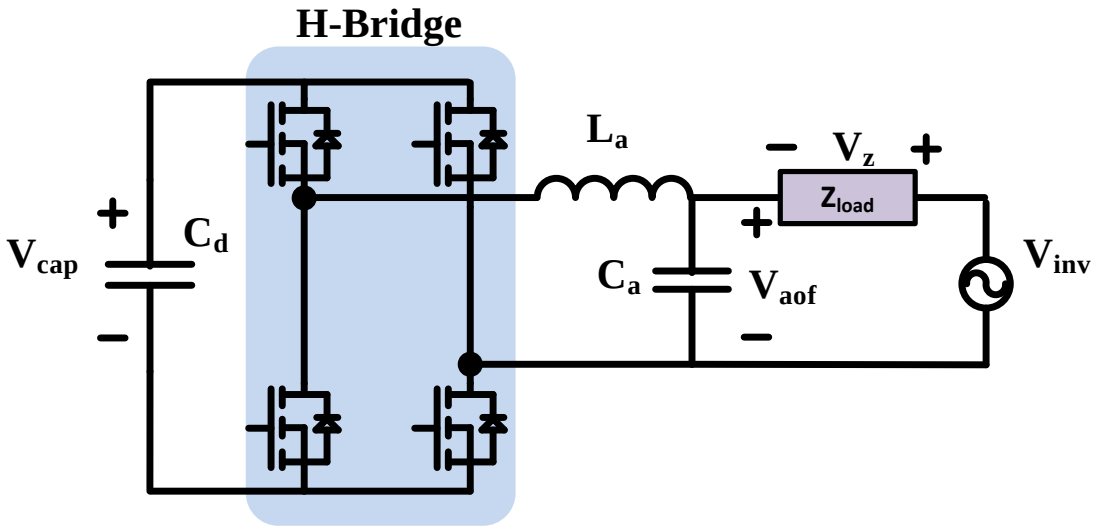

Fig. 2-1. Proposed AOF topology.

2.2.1 H-bridge

Traditionally, Si based MOSFET and IGBT can be used in H-bridge. Due to the high switching frequency realized in this AOF, wide-band gap device such as GaN FET is suitable for this application. Meanwhile, the power loss of GaN MOSFET is lower than the Si based MOSFET.

2.1.2 DC Link Capacitor

The DC link capacitor is used to maintain the DC voltage constant. The capacitor can be selected as the electrolytic capacitor which offers the large capacitor value and related small size. The voltage rating of DC link capacitor depends on the ASD inverter DC link value and induction motor structure.

2.1.3 Filter Inductor and Capacitor

A small high frequency inductor L_a is employed in AOF. This inductor can remove the high frequency harmonics from H-bridge switch. Due to the high frequency

operation, ferrite core is a good candidate material for L_a. One limitation of the ferrite core is the low saturation point through high current. Thanks to the small value of filter inductor, it can carry on high current without saturation [29]. As for filter capacitor C_a, it is also used for high frequency harmonics elimination. Due to AC voltage across C_a, a small value film capacitor is chosen here.

2.3 Control Strategy

The control block diagram for AOF is shown in Fig. 2-2. The controller consists of two loops. The outer loop is used to regulate the DC link voltage by employing PI control, while inner loop is achieved to control the AOF output voltage V_{aof}.

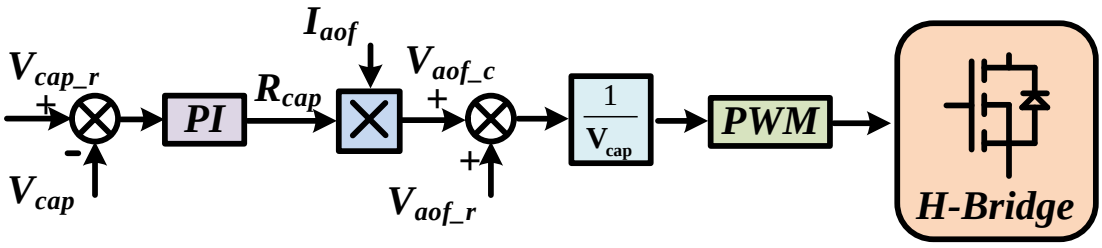

Fig. 2-2. Control scheme for the proposed AOF.

2.3.1 Outer Voltage Loop

For proper operation of AOF, it is necessary to maintain V_{cap} constant. V_{cap_r} can be set as the fixed value according to the inverter DC link value. In addition, voltage drop induced by AOF parasitic parameters must be compensated. In Fig. 2-2, the compensated voltage obtained by the virtual resistance R_{cap} multiplied by I_{aof} is added to V_{aof_r} in order to produce the reference signal.

In this thesis, the digital PI control is implemented by DSP. A standard equation of PI controller in the s domain is

$$G_{pi}(s) = K_p + K_i / s \tag{2-9}$$

For digital implementation, (2-9) is transferred to z domain

$$U_{pi}(z) = [K_p + K_i / (1 - z)]E(z) \tag{2-10}$$

Define $K_1 = K_p + K_i$ and $K_2 = -K_p$

$$U_{pi}(z) - z^{-1}U_{pi}(z) = [K_1 + K_2 z^{-1}]E(z) \tag{2-11}$$

Equation (2-11) can be rewritten as the difference equation as

$$u_{pi}(k) = u_{pi}(k-1) + K_1 e(k) + K_2 e(k-1) \tag{2-12}$$

which u_{pi} denotes the PI output value and e represents the error between voltage reference and sampled voltage.

According to (2-12), present state and previous state are both recorded to realize the iteration in the digital PI controller.

2.3.2 Inner Voltage Loop

The AOF reference voltage includes the V_{aof_r} and voltage drop compensation V_{aof_c}. Considering the control speed and complexity, here only the open loop is used. To generate the appropriate PWM signal, AOF reference voltage is divided by DC link voltage and then compared to the carrier waveforms.

2.4 Small Signal Model and Analysis

In order to design the stable feedback control, open-loop transfer function is introduced based on small signal model.

For bipolar PWM control strategy used in AOF, H-bridge output voltage V_o varies between -V_{cap} and V_{cap} in one cycle as shown in Fig. 2-3.

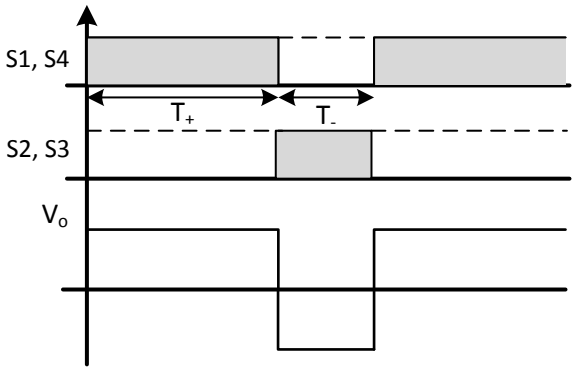

Fig. 2-3. Waveforms in one switching cycle.

In the positive half cycle, the state variables can be derived from Fig. 2-4.

$$L\dot{i}_L = V_{cap} - V_c - V_{inv} \tag{2-13}$$

$$C\dot{V} = i_L - \frac{V_c}{Z_o} \tag{2-14}$$

$$V_{aof} = V_{inv} + V_c \tag{2-15}$$

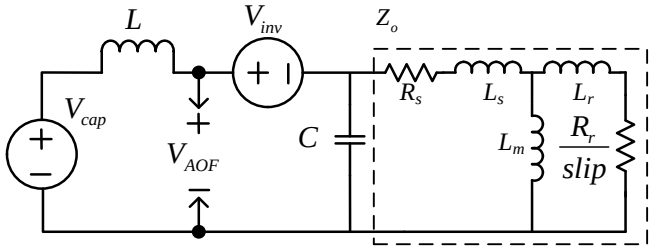

Fig. 2-4. Equivalent circuit in positive half cycle.

In the negative half cycle, the state variables can be derived from Fig. 2-5.

$$L\dot{i}_L = -V_{cap} - V_c - V_{inv} \tag{2-16}$$

$$C\dot{V}_c = i_L - \frac{V_c}{Z_o} \tag{2-17}$$

$$V_{aof} = V_{inv} + V_c \tag{2-18}$$

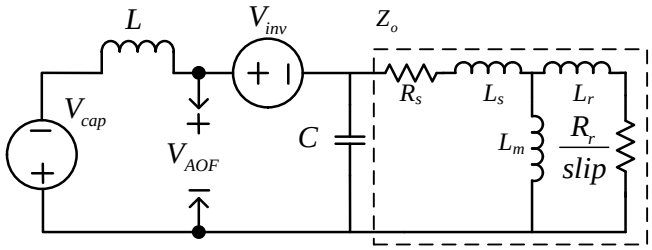

Fig. 2-5. Equivalent circuit in negative half cycle.

Integrating positive cycle and negative cycle, the state variables can be determined as

$$L\dot{i}_L = D(V_{cap} - V_c - V_{inv}) + D'(-V_{cap} - V_c - V_{inv}) \tag{2-19}$$

$$C\dot{V}_c = D(i_L - \frac{V_c}{Z_o}) + D'(i_L - \frac{V_c}{Z_o}) \tag{2-20}$$

$$V_{aof} = D(V_{inv} + V_c) + D'(V_{inv} + V_c) \tag{2-21}$$

Introducing the small signal disturbance, the state variables can be rewritten as

$$L(\dot{i}_L + \hat{\dot{i}}_L) = (D + \hat{d})(V_{cap} + \hat{v}_{cap} - V_c - \hat{v}_c - V_{inv} - \hat{v}_{inv}) + D'(-V_{cap} - \hat{v}_{cap} - V_c - \hat{v}_c - V_{inv} - \hat{v}_{inv}) \tag{2-22}$$

$$C(\dot{V}_c + \hat{\dot{V}}_c) = (D + \hat{d})(i_L + \hat{i}_L - \frac{V_c}{Z_o} - \frac{\hat{v}_c}{Z_o}) + (D' - \hat{d})(i_L + \hat{i}_L - \frac{V_c}{Z_o} - \frac{\hat{v}_c}{Z_o}) \tag{2-23}$$

$$V_{aof} + \hat{v}_{aof} = (D + \hat{d})(V_{inv} + \hat{v}_{inv} + V_c + \hat{v}_c) + D'(V_{inv} + \hat{v}_{inv} + V_c + \hat{v}_c) \tag{2-24}$$

Only consider the first-order ac terms on both sides, hence:

$$L\dot{\hat{i}}_L = (2D-1)\hat{v}_{cap} - \hat{v}_c - \hat{v}_{inv} + 2V_{cap}\hat{d} \tag{2-25}$$

$$C\dot{\hat{V}}_c = \hat{i}_L - \frac{\hat{v}_c}{Z_o} \tag{2-26}$$

$$\hat{v}_{aof} = \hat{v}_{inv} + \hat{v}_c \tag{2-27}$$

Small signal model shown in Fig. 2.6 can be constructed based on the state variables above. Fig. 2-6(a) represents the inductor current loop. The terms $(2D-1)\hat{v}_{cap}$, $\hat{v}_c$ and $\hat{v}_{inv}$ are voltage control voltage sources. The term $2V_{cap}\hat{d}$ is determined only by the duty cycle variations and can be considered as the independent voltage source. Fig. 2-6(b) shows the small signal model for the voltage loop. $\hat{i}_L$ and $\hat{v}_c / Z_o$ are both dependent current sources. Fig. 2-6(c) is the small signal model for the load loop, in which $\hat{v}_{inv}$ and $\hat{v}_c$ are both voltage control voltage sources.

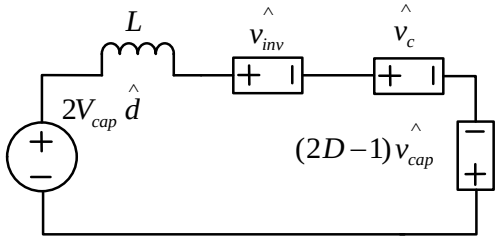

(a)

Fig. 2-6. Small signal model for AOF.

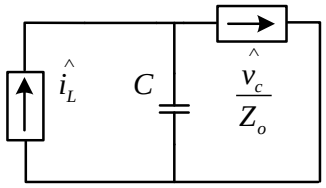

(b)

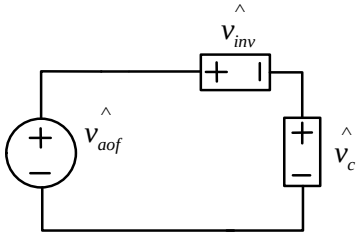

(c)

Fig. 2-6 Continued.

The state variables can be written in the following matrix form:

$$\begin{bmatrix} \dot{\hat{v}}_C \\ \dot{\hat{i}}_L \\ \dot{\hat{v}}_{inv} \\ \dot{\hat{v}}_{cap} \end{bmatrix} = A \begin{bmatrix} \hat{v}_c \\ \hat{i}_L \\ \hat{v}_{inv} \\ \hat{v}_{cap} \end{bmatrix} + B\hat{d}$$

$$\hat{v}_{aof} = C \begin{bmatrix} \hat{v}_c \\ \hat{i}_L \\ \hat{v}_{inv} \\ \hat{v}_{cap} \end{bmatrix}$$

In this two matrixes

$$A=\begin{bmatrix} -\frac{1}{Z_o C} & \frac{1}{C} & 0 & 0 \\ -\frac{1}{L} & 0 & -\frac{1}{L} & \frac{2D-1}{L} \\ 0 & 0 & 0 & 0 \\ 0 & 0 & 0 & 0 \end{bmatrix}$$

$$B=\begin{bmatrix} 0 \\ \frac{2V_{cap}}{L} \\ 0 \\ 0 \end{bmatrix}$$

$$C=\begin{bmatrix} 1 & 0 & 1 & 0 \end{bmatrix}$$

Therefore, the control-output transfer function can be derived as

$$\frac{\hat{v}_{aof}}{\hat{d}} = C(sI-A)^{-1}B \tag{2-28}$$

Solve the above equation.

$$G_{vd}(s)=\frac{\hat{v}_{aof}}{\hat{d}}=\frac{2V_{cap}Z_o}{CLZ_o s^2+Ls+Z_o} \tag{2-29}$$

2.5 Conclusion

The proposed AOF is introduced in this section. An H-bridge GaN based topology is employed to implement harmonic injection. The component of AOF is

detailed and control strategy is discussed. Based on the small signal model, the controller can be designed to achieve system stability.

3. SINGLE PHASE ASD WITH ACTIVE OUTPUT FILTER

The proposed AOF aims to further mitigate acoustic noise and reduce the size for ASD system. Several industry areas such as shipboard, electric vehicle and submarine have the strict requirement for the acoustic noise. Therefore, the proposed ASD is of special interest to these areas. In this Section, single-phase ASD with AOF is introduced. The simulation and experimental results demonstrate the advantage of AOF for acoustic noise reduction.

3.1 System Configuration

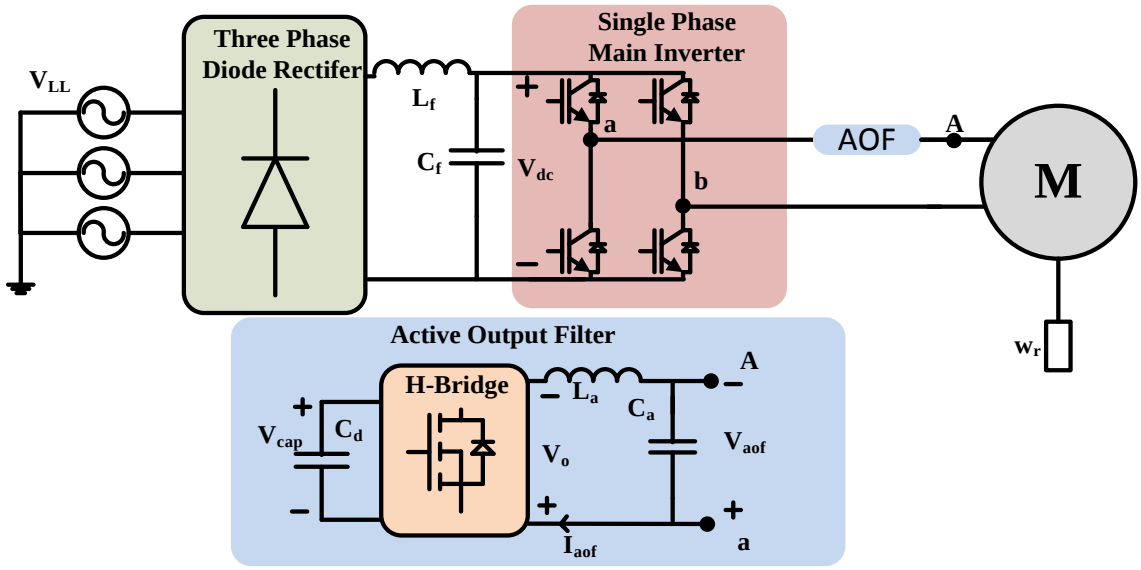

Fig. 3-1. Single-phase ASD system with the proposed AOF.

The power stage of the single-phase ASD system with AOF is shown in Fig. 3-1. IGBT based single-phase inverter operates at low switching frequency (2.1 kHz) based on SPWM strategy. According to (2-7), the AOF output voltage V_{aof} can be derived as

$$V_{aof} = V_{ab} - V_{Ab} = V_{ab} - MV_{dc}\cos(w_0 t) \tag{3-1}$$

V_{ab} given by (3-2) denotes the single-phase inverter output voltage using naturally sampled reference and unipolar SPWM [30].

$$V_{ab} = V_{dc} M \cos(\omega_0 t) + \frac{4V_{dc}}{\pi} \sum_{m=1}^{\infty} \sum_{n=-\infty}^{\infty} \frac{1}{m} J_n(m\pi M) \sin(n\frac{\pi}{2}) \cos[(m\omega_{\text{inv}} \pm n\omega_0)t] \quad (3\text{-}2)$$

In the practical digital controller, V_{ab} is generated by main inverter switching function.

$$V_{ab} = V_{dc}(S_a - S_b) \quad (3\text{-}3)$$

where S_a and S_b denote switching function of leg A and leg B, respectively.

According to (3-1) and (3-2), V_{aof} can be rewritten as

$$V_{aof} = \frac{4V_{dc}}{\pi} \sum_{m=1}^{\infty} \sum_{n=-\infty}^{\infty} \frac{1}{m} J_n(m\pi M) \sin(n\frac{\pi}{2}) \cos[(m\omega_{\text{inv}} \pm n\omega_0)t] \quad (3\text{-}4)$$

Equation (3-4) can be used as the reference voltage for H-Bridge modulation. Assuming modulation index of H-Bridge m_{a_h}=1, the minimum value of DC link voltage V_{cap} can be determined by

$$V_{cap} = \frac{1}{m_{a\_h}} \max_{t=0}^{\infty} (\frac{4V_{dc}}{\pi} \sum_{m=1}^{\infty} \sum_{n=-\infty}^{\infty} \frac{1}{m} J_n(m\pi M) \sin(n\frac{\pi}{2}) \cos[(m\omega_{\text{inv}} \pm n\omega_0)t]) = V_{dc} \quad (3\text{-}5)$$

The switching function for H-bridge can be derived from

$$S_{aof} = \frac{\frac{4V_{dc}}{\pi} \sum_{m=1}^{\infty} \sum_{n=-\infty}^{\infty} \frac{1}{m} J_n(m\pi M) \sin(n\frac{\pi}{2}) \cos[(m\omega_{\text{inv}} \pm n\omega_0)t]}{V_{dc}} \quad (3\text{-}6)$$

3.2 Design Example

A 1/2 horsepower rated single-phase ASD system is designed to verify the operation principle of the proposed AOF. The operation specifications are shown in Table 3-1.

Table 3-1: Single-phase ASD with AOF operation condition

Description	Value
Input line-line voltage V_{LL}	240V
Intermediate DC voltage V_{dc}	324V
Rated output power P_o	1/2hp
Main switching frequency f_{inv}	2.1kHz
AOF switching frequency f_s	48kHz
DC link voltage V_{cap}	324V
Rated stator voltage V_{Ab}	120V
Rated frequency f_o	60Hz
Rated stator current I_A	6.8A

3.2.1 Parameter Design of AOF

Considering the interval in which V_o equals to V_{cap}, the voltage of L_a can be expressed as

$$V_{La}(t) = L_a \frac{\Delta I_{pp}}{D(t)T_s} = V_{cap} - V_{aof}(t) \tag{3-7}$$

Becuase switching frequency of AOF is much higher than the harmonic frequency of interest, the V_{aof} can be averaged as

$$V_{aof}(t) \approx V_{o\_avg}(t) \tag{3-8}$$

Then substituting (3-8) into (3-7)

$$L_a = \frac{T_s}{\Delta I_{pp}} \frac{V_{aof}(t)}{V_{cap}} (V_{cap} - V_{aof}(t)) \tag{3-9}$$

Differentiating (3-9) with respect to $V_{aof}(t)$, the maximum value of L_a is determined when $V_{aof}(t) = \frac{1}{2} V_{cap}$.

$$L_a \le \frac{V_{cap} T_s}{4\Delta I_{pp\_\max}} \tag{3-10}$$

The reactive power in filter capacitor C_a should be lower than 10% of the output power [31].

$$C_a \le 0.1 \times \frac{P_e}{6\pi f_o V_{Ab}^2} \tag{3-11}$$

In (3-11), P_e is the electrical power which can be achieved as

$$P_e = \frac{P_o}{\eta} \tag{3-12}$$

where η represents power efficiency of induction motor.

In addition, the resonant frequency of the filter should be satisfied as [32].

$$10 f_{inv} < \frac{1}{2\pi\sqrt{L_a C_a}} < \frac{1}{2} f_s \tag{3-13}$$

where f_s represents switching frequency of AOF.

Assuming no power loss in AOF, the DC link current is the product of switching function and AOF output current.

$$I_{cap}(t) = S_{aof} I_{aof}(t) \tag{3-14}$$

Due to AOF in series with the load, $I_{aof}(t)$ is equivalent to the load current.

$$I_{aof}(t) = \sqrt{2} I_A \cos(wt) \tag{3-15}$$

Integrating (3-6), (3-14) and (3-15), $I_{cap}(t)$ can be defined as

$$I_{cap}(t) = \frac{\sqrt{2}}{V_{cap}} \frac{4V_{dc}}{\pi} \sum_{m=1}^{\infty} \sum_{n=-\infty}^{\infty} \frac{1}{m} J_n(m\pi M) \sin(n\frac{\pi}{2}) \cos[(m\omega_{\text{inv}} \pm n\omega_0)t] \tag{3-16}$$

Considering the positive half cycle of H-bridge $T_+ = DT_s$, the

$$\Delta Q = \int_{T_1}^{T_1+D(t)T_s} I_{cap}(t)dt = C_d \Delta V_{cap} \tag{3-17}$$

Substituting (3-17) into (3-16), the minimum value of C_d can be defined as:

$$C_d \geq \frac{\sqrt{2} I_A T_s}{\omega \Delta V_{cap\_\min}} \max[\sin(\omega T_1 + \omega T_s) - \sin \omega T_1] \tag{3-18}$$

Because switching cycle of H-bridge T_s is a very small interval compared to output current cycle, (3-18) can be rewritten as

$$C_d \geq \frac{\sqrt{2} I_A T_s}{\omega \Delta V_{cap\_\min}} \max(\frac{d \sin(\omega t)}{d\omega}) \tag{3-19}$$

Due to $\frac{dsin(\omega t)}{dt} = \omega cos(\omega t)$, it is not difficult to find $\max\left(\frac{dsin(\omega t)}{dt}\right) = \omega$. Therefore, DC link capacitor C_d can be determined in accordance with the limit of DC link voltage ripple.

$$C_d \geq \frac{\sqrt{2} I_{A(B,C)} T_s}{\Delta V_{d\_\max}} \tag{3-20}$$

Based on the equations above and Table 3-1, the AOF parameters can be calculated as shown in Table 3-2.

3.2.2 LC Passive Filter

In order to do the comparison between AOF and LC passive filter, value of LC passive filter is calculated based on [33].

$$L_a \geq \frac{1}{8} \frac{V_{dc}}{0.2\sqrt{2} I_A f_{inv}} - L_{motor} \tag{3-21}$$

$$C_a \leq 0.1 \times \frac{P_e}{2\pi f_o V_{Ab}^2} \tag{3-22}$$

In (3-21), L_{motor} represents the inductor value in the induction motor equivalent circuit as shown in Fig. 3-2 (ω is the fundamental angular frequency).

$$Z_{motor} = R_{motor} + j\omega L_{motor} = R_s + j\omega L_s + \frac{-\omega^2 L_r L_m slip + j\omega L_m R}{j\omega(L_r + L_m)slip + R_r} \tag{3-23}$$

$$L_{motor} = L_s + \frac{L_m R_r^2 + \omega^2 (L_r + L_m) L_r L_m slip^2}{\omega^2 (L_r + L_m)^2 slip^2 + R_r^2} \tag{3-24}$$

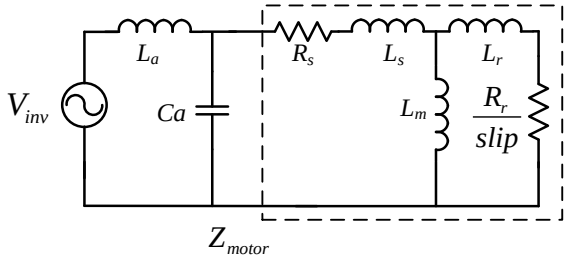

Fig. 3-2. Single-phase ASD equivalent circuit with passive filter.

According to Table 3-1, (3-21) and (3-22), specifications of LC filter are listed in Table 3-2.

Table 3- 2: Specifications of LC filter and AOF in single-phase ASD

Description	**LC Filter**	**AOF**
Filter Capacitor C_a	33μF	15μF
Filter Inductor L_a	3.2mH	68μH
DC Link Capacitor C_d	N/A	500μF

3.2.3 Volume Comparison

In order to compare the power density of AOF and LC filter, the volume of the components should be explored in detail.

The value of capacitor is derived as

$$C = \frac{\varepsilon A}{d} = \frac{\varepsilon V_{v\_c}}{d^2} \tag{3-25}$$

where ε, V_{v_c} and d denote dielectric permittivity, volume and layer thickness, respectively.

Considering capacitor voltage approximately proportional to the dielectric layer thickness [34], (3-25) is rewritten as

$$V_{v\_c} = \frac{C(kV)^2}{\varepsilon} \tag{3-26}$$

In (3-26), it is assumed that $k \approx 5nm/V$ and $\varepsilon \approx 10 \times 10^{-11}\mathrm{F/m}$ for the aluminum electrolytic capacitor and $k \approx 10nm/V$ and $\varepsilon \approx 3 \times 10^{-11}\mathrm{F/m}$ for the film capacitor. Therefore, the capacitor volume in AOF and LC filter can be estimated as shown in Table 3-3.

The value of inductor is given by

$$L = \frac{\mu n^2 V_{v\_l}}{l^2} \tag{3-27}$$

where μ, V_{v_l}, n and l denote permeability, inductor core volume, air gap length and turns, respectively.

According to Ampere's Law, the magnetic flux density in the inductor is obtained as

$$B_{\max} = \frac{\sqrt{2}\mu n I_A}{l} \tag{3-28}$$

Integrating (3-27) and (3-28)

$$V_{v\_l} = \frac{2L\mu I^2{}_A}{B_{\max}} \tag{3-29}$$

Assuming the inductor core is implemented by ferrite cores, it can be achieved thatμ ≈ $2000 \times 4\pi \times 10^{-7}$H/m. If $B_{max} = 0.3T$, the inductor volume can be estimated based on (3-29), which is listed in Table 3-3.

Table 3- 3: Volume comparison of LC filter and AOF in single-phase ASD

Description	LC Filter	AOF
Volume of C_a	2.1cm^3	0.9cm^3
Volume of L_a	1479cm^3	52cm^3
Volume of C_{cap}	N/A	5.6cm^3
Volume of H-bridge and gate driver	N/A	35.1cm^3
Overall Volume	1481.2cm^3	93.6cm^3

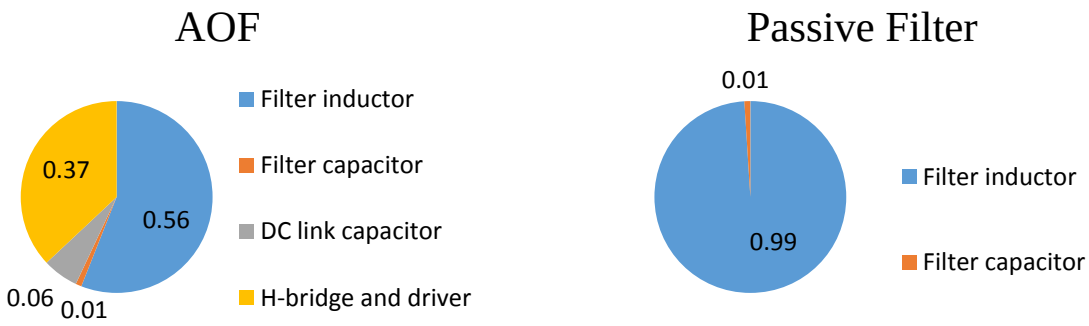

Fig. 3-3. Volume distribution.

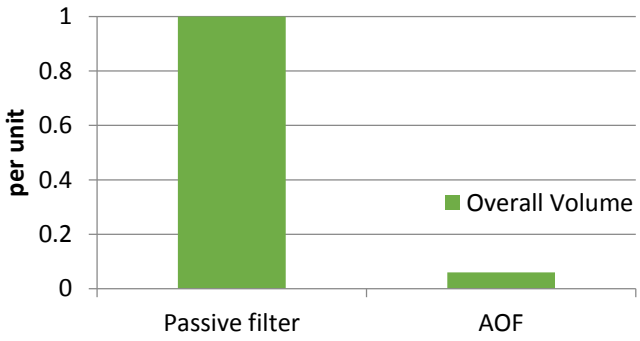

Fig. 3-4. Overall volume comparison.

Fig. 3-3 shows the inductor accounts for most of the volume in both of passive filter and AOF. Owing to the much smaller inductor employed in AOF, the overall volume of AOF reduces to about 6.5% of LC filter as shown in Fig. 3-4. Note practical capacitor and inductor volume may be slightly different from the theoretic value.

3.2.4 Transfer Function

According to (2-29) and Table 3.1 – 3.2, the single-phase AOF control-output transfer function can be expressed as:

$$G_{vd}(s) = \frac{\hat{v}_{aof}}{\hat{d}} = \frac{7.8s + 10920}{1.22\times10^{-11}s^3 + 1.71\times10^{-8}s^2 + 0.01s + 16.8} \tag{3-30}$$

The pole-zero plot is shown in Fig. 3-5. Because all of poles are located in the left half plane, it can achieve the stability. However, the stability margin is not enough due to p1 and p2 close to the imaginary axis.

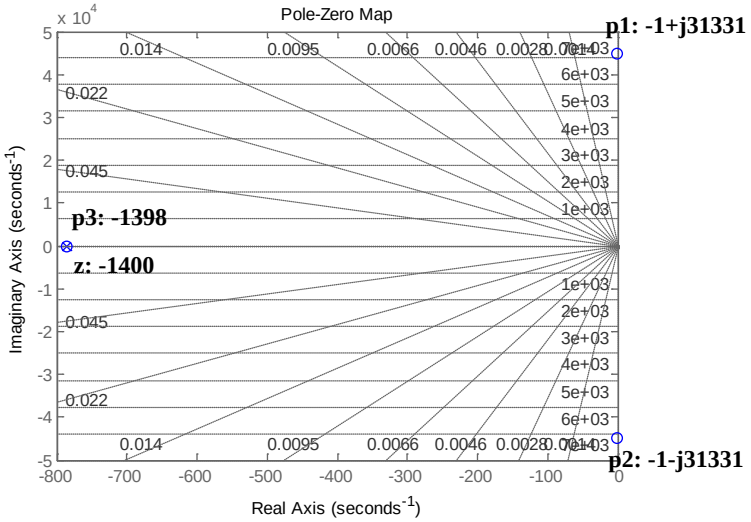

Fig. 3-5: Pole-zero map of single-phase AOF control-output transfer function.

3.3 Simulation Results

(1) Steady state operation

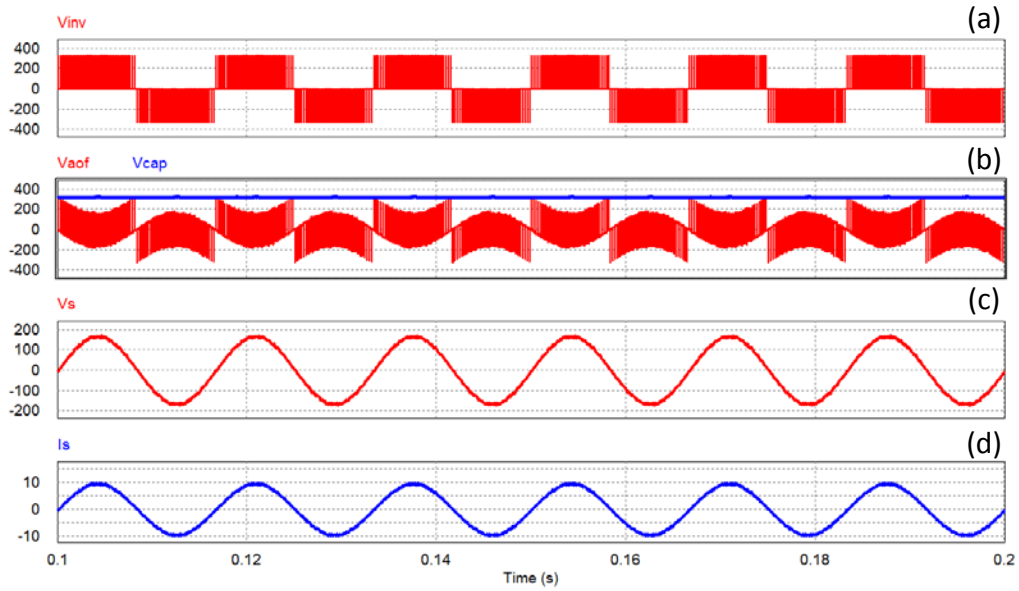

Fig. 3-6. Single-phase ASD with AOF in 120V/60Hz steady state operation. (a) Inverter output voltage. (b) AOF output voltage and DC link voltage. (c) Stator voltage. (d) Stator current.

First, the single-phase ASD system with AOF is simulated in the 120V/60Hz steady state condition based on PSIM. Fig. 3-6 shows the key waveforms in the rating condition. In Fig. 3-6(a), inverter output voltage is the unipolar PWM waveforms. Fig. 3-6(b) shows the DC link voltage keeps constant at about 325V, which validates the DC link voltage is equivalent to intermediate stage DC voltage. In addition, the maximum value of AOF output voltage is the same as DC link voltage due to the modulation index m_{a_h}=1. Fig. 3-6(c) illustrates the stator voltage is almost pure sinusoidal waveforms and the magnitude is 120V. Similarly, Fig. 3-6(d) shows stator current is the 60Hz sinusoidal

waveform and the magnitude is 6.8A. Both of stator voltage and current are in accordance with Table 3-1.

(2) Load step operation

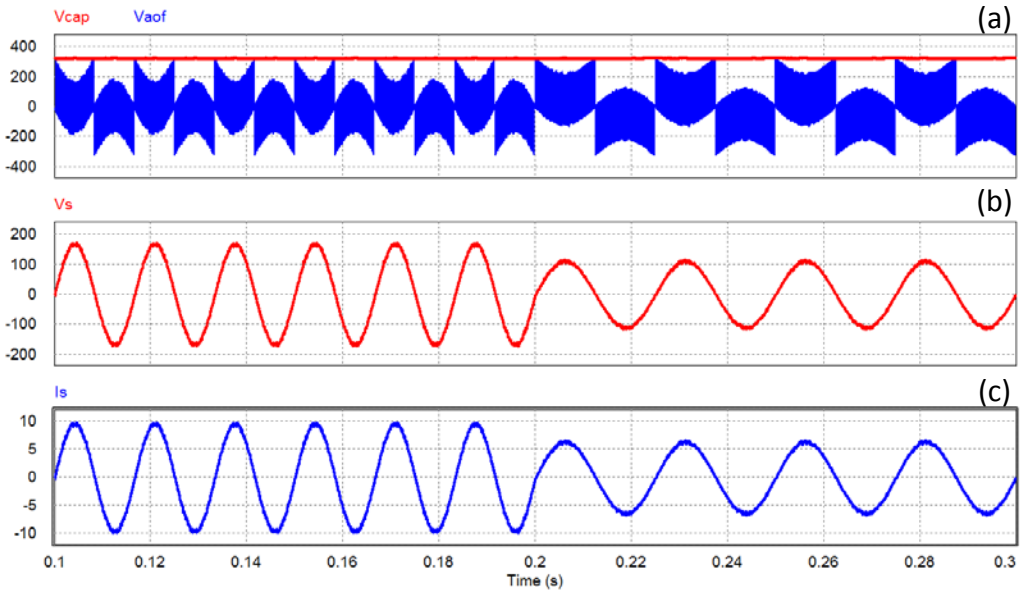

Fig. 3-7. Single-phase ASD with AOF in load step operation. (a) AOF output voltage and DC link voltage. (b) Stator voltage. (c) Stator current.

In Fig. 3-7(a), DC link voltage V_{cap} is nearly constant at 325V during the transition. In addition, amplitude and frequency of AOF output voltage V_{aof} varies with the load transition, which verifies the dynamic tuning of AOF. In Fig. 3-7(b), stator voltages change from 120V/60Hz to 80V/40Hz, which demonstrates the constant V/Hz operation. The stator current steps down with the stator voltage as shown in Fig. 5-7(c).

(3) Line voltage step operation

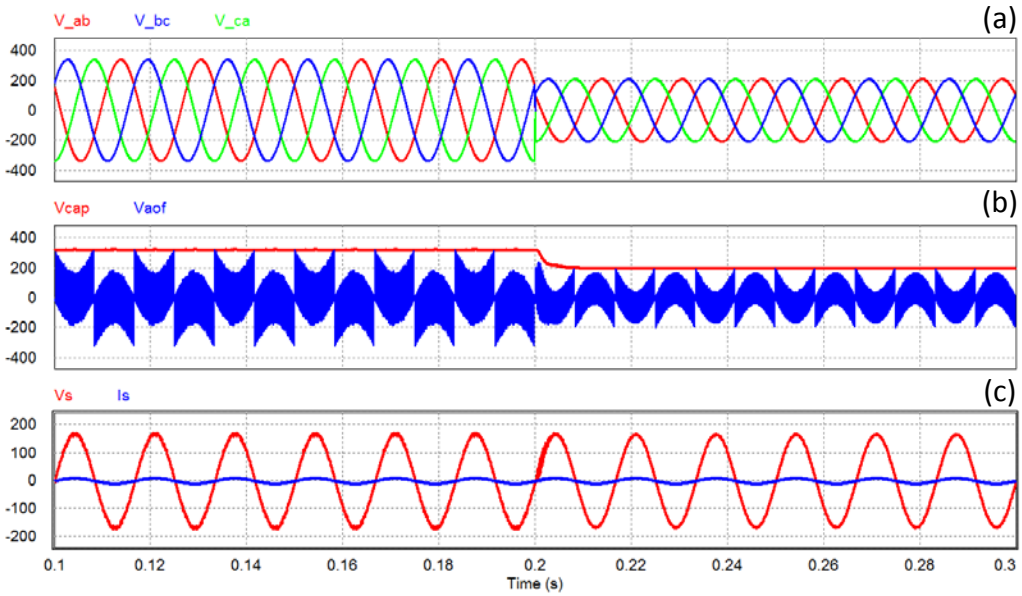

Fig. 3-8. Single-phase ASD with AOF in line step operation. (a) Three phase line voltage. (b) AOF output voltage and DC link voltage. (c) Stator voltage and current.

The line transient operation is shown in Fig. 3-8. It can be observed that stator voltage keeps constant at 120V/60Hz during line step transition when grid voltage decreases from 240V to 150V. In addition, the DC link voltage of AOF changes with the intermediate DC voltage which is proportional to line voltage determined by (1-1).

(4) Harmonics comparison between LC filter and AOF

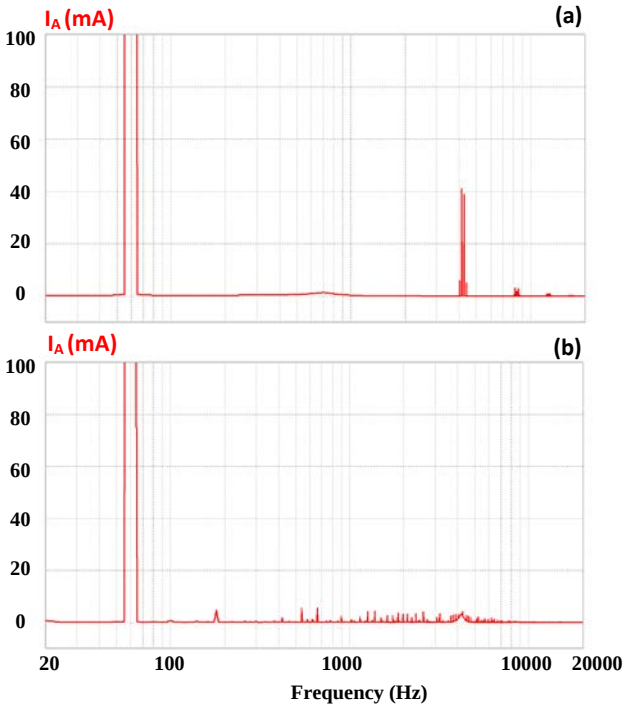

Fig. 3-9. FFT analysis of stator current harmonics at 120V/60Hz condition. (a) Single phase ASD with LC filter. (b) Single phase ASD with AOF.

To verify the AOF advantage of harmonic elimination, the stator current harmonics comparison between LC filter and AOF is shown in Fig. 3-9. In the range of 20 ~ 20k Hz (audible frequency range), stator current harmonics in ASD with the proposed AOF are much lower than LC filter, especially around the 2nd switching frequency.

3.4 Experimental Results

The experimental specifications are detailed in Table 3-4. Digital control is implemented by DSP C2000 and the prototype is shown in Fig. 3-10.

Table 3-4: Single phase ASD with AOF experimental specifications

Description	Value
Intermediate DC voltage	200V
Rated output power P_o	1/2hp
Main switching frequency f_{inv}	2.1kHz
AOF switching frequency f_s	48kHz
DC link voltage V_{cap}	200V
Rated stator voltage V_{Ab}	120V
Rated frequency f_o	60Hz
Rated stator current I_A	6.8A

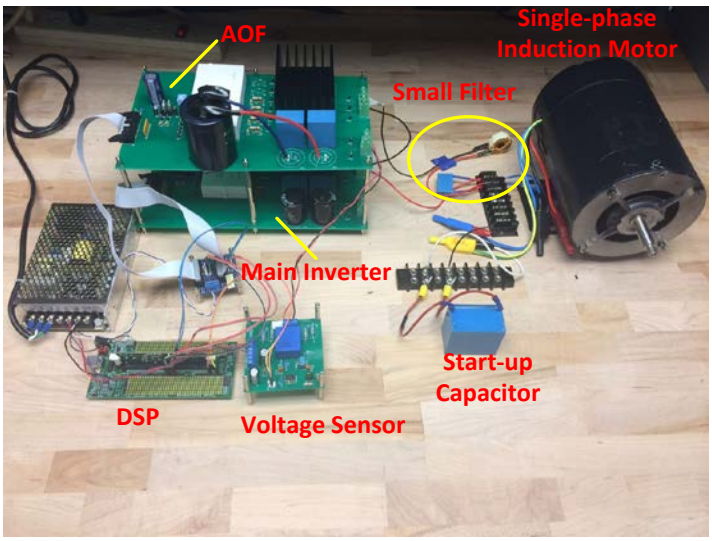

Fig. 3-10. Prototype setup for ½ hp single-phase ASD with AOF.

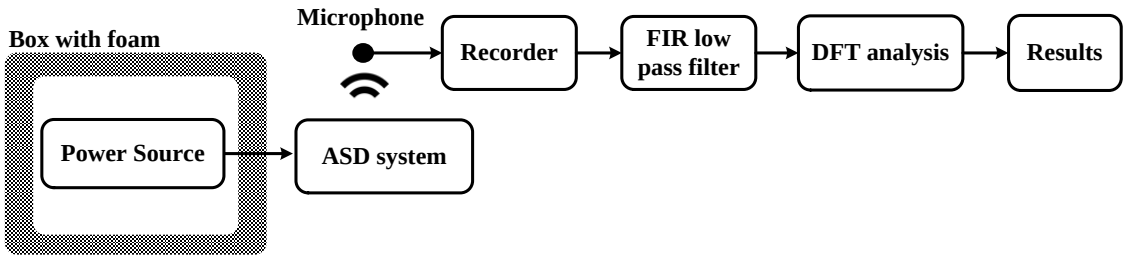

Fig. 3-11. Block diagram of acoustic noise measurement system.

The overall acoustic noise measurement system is shown in Fig. 3-11. In order to mitigate the noise from power source, power source is installed in the box with foam. Microphone is located in 0.5m away from the ASD system. Then, the collected acoustic

noise about 5 second duration is stored in the recorder. A digital FIR low pass filter based on Matlab toolbox is used to allow only audible frequency signals passing. This filter is designed with the cut-off frequency of 20 kHz and stopband attenuation is about -80 dB/dec. Last, by using discrete fourier analysis (DFT) in Matlab, the acoustic noise spectra is achieved shown in the following experimental results.

(1) 80V/40Hz Operation Condition

First, the prototype operating at 80V/40Hz is tested as shown in Fig. 3-12 ~ Fig. 3-16. By using AOF, the stator voltage only includes the fundamental frequency voltage as shown in Fig. 3-12, and hence, there is no voltage overshoot in the motor terminal. In the same figure, the DC link voltage V_{cap} keeps constant at about V_{dc}, which is in accordance with the theory analysis. The waveform of AOF output voltage has the good agreement with the simulation result.

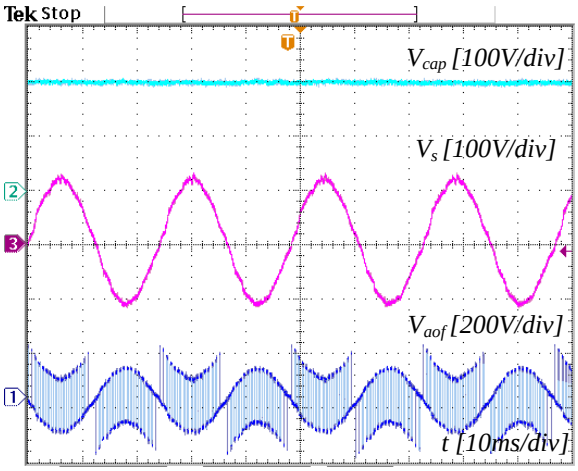

Fig. 3-12. Single phase ASD with AOF at 80V/40Hz condition. Ch1: AOF output voltage. Ch2: AOF DC link voltage. Ch3: Stator voltage.

Fig. 3-13 and Fig. 3-14 illustrate the stator current harmonics comparison between LC filter and AOF. It can be observed that current harmonics are much lower by using AOF, especially for harmonics around low switching frequency sidebands.

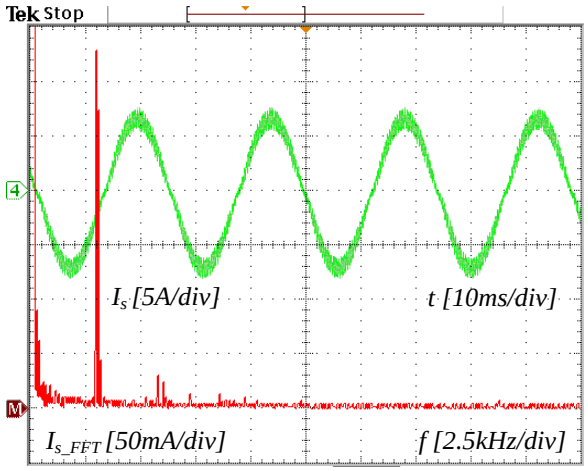

Fig. 3-13. Single phase ASD with passive filter at 80V/40Hz condition. Ch4: Stator current. ChM: FFT analysis of stator current.

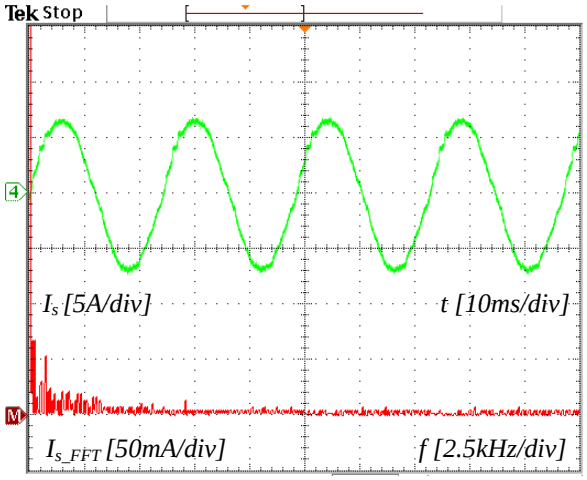

Fig. 3-14. Single phase ASD with AOF at 80V/40Hz condition. Ch4: Stator current. ChM: FFT analysis of stator current.

Fig. 3-15 demonstrates the acoustic noise spectrum in the induction motor with passive filter, in which some noise spikes are distributed around 2nd order switching frequency. It proves the analysis in Section 2 that current harmonics in low switching frequency cause the corresponding acoustic noise peaking. However, by using AOF, these noise spikes are dramatically suppressed shown in Fig. 3-16. In this case, the dominant area of acoustic noise is only arranged in the fundamental frequency.

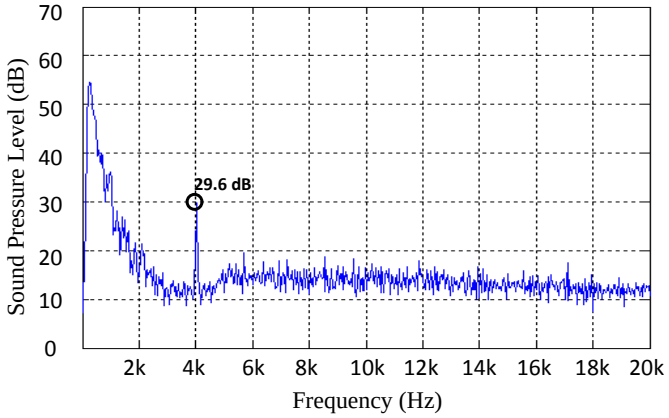

Fig. 3-15. Acoustic noise spectrum of single phase ASD with passive filter at 80V/40Hz condition (inverter switching frequency is 2.1 kHz).

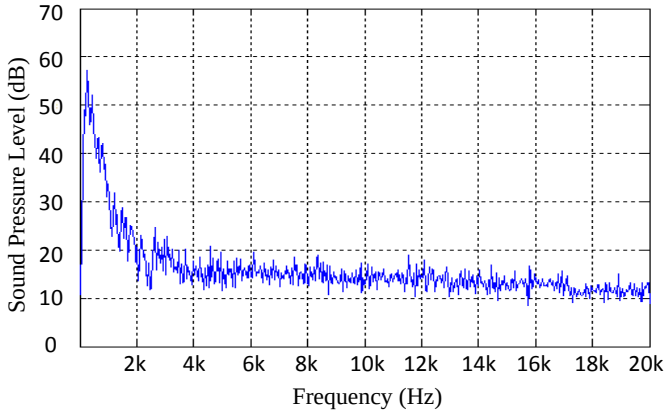

Fig. 3-16. Acoustic noise spectrum of single phase ASD with AOF at 80V/40Hz condition (inverter switching frequency is 2.1 kHz).

(1) 120V/60Hz Operation Condition

The 120V/60Hz operation condition (rated condition) is also measured as shown in Fig. 3-17 ~ Fig. 3-21. Fig. 3-17 illustrate AOF removes most of harmonics from PWM mode inverter and provides the almost sinusoidal waveforms at the motor terminal. In addition, DC link voltage in 120V/60Hz condition (Fig. 3-17) equals to 80V/40Hz condition (Fig. 3-12) due to invariant intermediate DC voltage V_{dc}.

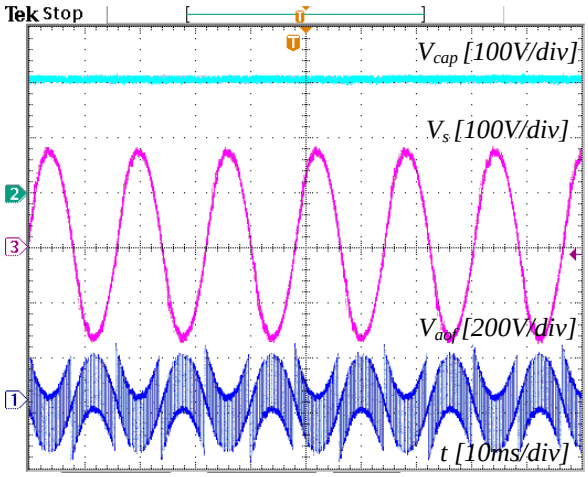

Fig. 3-17. Single phase ASD with AOF at 120V/60Hz condition. Ch1: AOF output voltage. Ch2: AOF DC link voltage. Ch3: Stator voltage.

Fig. 3-18 shows the stator current harmonics using LC filter, which are mainly distributed in second and fourth order switching frequency sidebands. In similar with 80V/40Hz condition, AOF operating at 120V/60Hz can also efficiently lower the stator current harmonics as shown in Fig. 3-19.

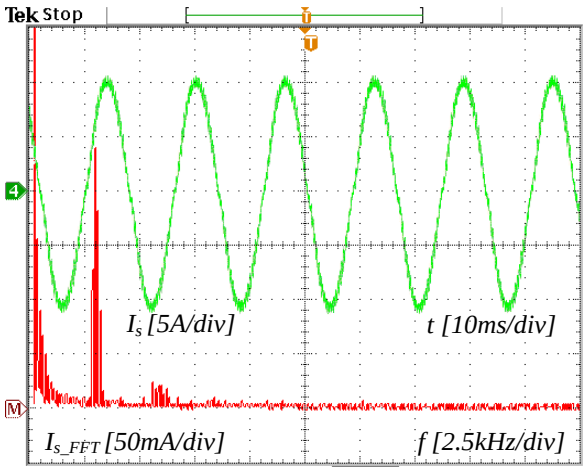

Fig. 3-18. Single phase ASD with passive filter at 120V/60Hz condition. Ch4: Stator current. ChM: FFT analysis of stator current.

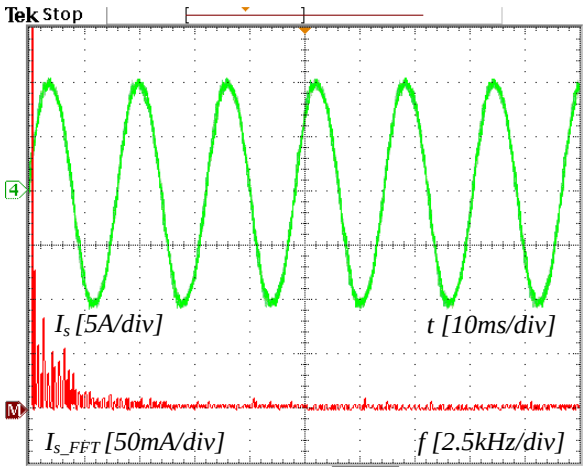

Fig. 3-19. Single phase ASD with AOF at 120V/60Hz condition. Ch4: Stator current. ChM: FFT analysis of stator current.

Corresponding to stator current harmonics spectrum shown in Fig. 3-18, some noise spikes occur at low switching frequency sidebands by using LC filter, which is presented in Fig. 3-20. In similar with 80V/40Hz condition, these noise spikes are also eliminated due to AOF at 120V/60Hz condition shown in Fig. 3-21.

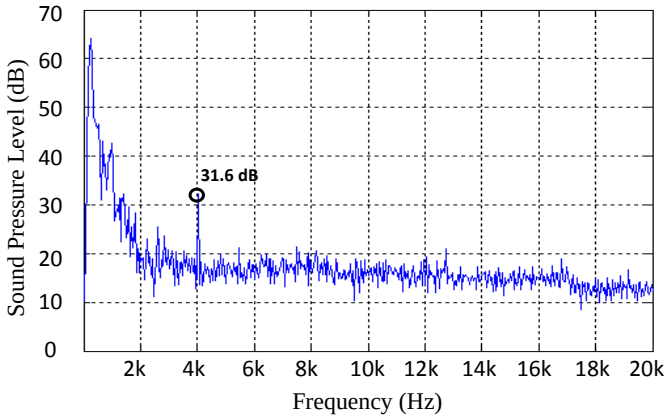

Fig. 3-20. Acoustic noise spectrum of single phase ASD with passive filter at 120V/60Hz condition (inverter switching frequency is 2.1 kHz).

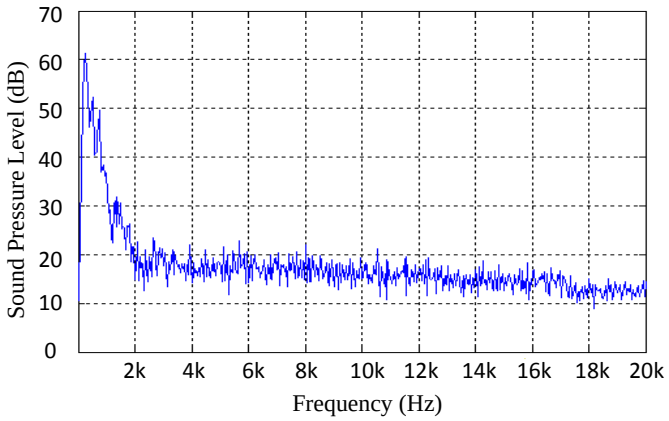

Fig. 3-21. Acoustic noise spectrum of single phase ASD with AOF at 120V/60Hz condition (inverter switching frequency is 2.1 kHz).

The overall acoustic noise of single-phase ASD system is presented in Fig. 3-22. Compared to LC filter, acoustic noise is reduced at least 0.6 dB at different operation conditions.

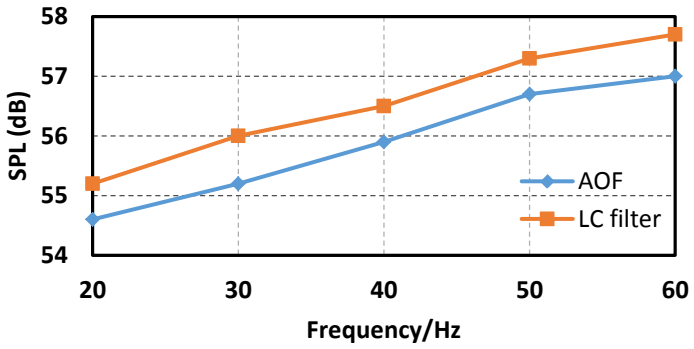

Fig. 3-22. Overall noise emitted by single-phase ASD at various fundamental frequencies operation conditions.

3.5 Conclusion

In this section, the proposed AOF is applied in the single phase ASD system. The overall system configuration along with the design methodology for components is discussed. The advantage of AOF is validated by the simulation and experimental results.

4. THREE PHASE ASD WITH ACTIVE OUTPUT FILTER

In addition to single-phase ASD, the proposed AOF can be also applied in the three phase ASD. In the three phase ASD system, three AOFs are plugged in every phase to replace the LC filter. Three AOFs are controlled separately using the double loop strategy discussed in Section 2.

4.1 System Configuration

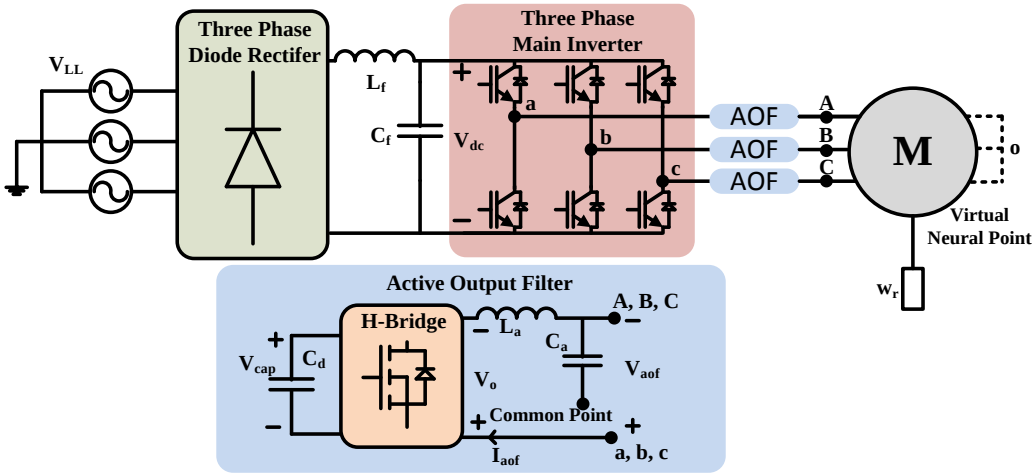

Fig. 4-1. Three-phase ASD system with the proposed AOF.

The power stage of the three-phase ASD system with AOF is shown in Fig. 41. Three-phase diode rectifier converts the three-phase AC voltage to DC voltage. L_f and C_f are used to mitigate the DC voltage ripple. IGBT based three-phase inverter operates at low switching frequency (2.1 kHz) based on space vector PWM (SVPWM) strategy. According to (2-7), the AOF output voltage V_{aof} can be derived as

$$V_{aof} = V_{ab} - V_{Ab} = V_{ab} - MV_{dc}\cos(w_0 t) \tag{4-1}$$

$V_{ao(bo,co)}$ given by (4-2) denotes the virtual line-neural voltage of three-phase inverter [30].

$$V_{ao(bo,co)} = V_{dc}\frac{M}{2}\cos(\omega_0 t) + \sum_{m=0}^{\infty}\sum_{n=1}^{\infty} A_{mn}\cos[(m\omega_{\text{inv}} \pm n\omega_0)t] \tag{4-2}$$

where ω_o and ω_{inv} denote fundamental angular frequency and three-phase inverter switching angular frequency, respectively. In addition, A_{mn} can expressed as

$$\begin{aligned} A_{mn} = {} & \frac{8V_{dc}}{m\pi^2}\{\frac{\pi}{6}\sin[(m+n)\frac{2}{\pi}][J_n(m\frac{3\pi}{4}M) + 2\cos(n\frac{\pi}{6})J_n(m\frac{\sqrt{3}\pi}{4}M)] + \\ & \frac{1}{n}\sin(m\frac{\pi}{2})\cos(n\frac{\pi}{2})\sin(n\frac{\pi}{6})[J_0(m\frac{3\pi}{4}M) - J_0(m\frac{\sqrt{3}\pi}{4}M)]|_{n\neq 0} + \\ & \sum_{k=1}^{\infty}\frac{1}{n+k}\sin[(\mathrm{m}+\mathrm{k})\frac{\pi}{2}]\cos[(\mathrm{n}+\mathrm{k})\frac{\pi}{2}]\sin[(\mathrm{n}+\mathrm{k})\frac{\pi}{6}]\bullet \\ & \{[J_n(m\frac{3\pi}{4}M) + 2\cos[(2n+3k)\frac{\pi}{6}]J_k(m\frac{\sqrt{3}\pi}{4}M)\} \end{aligned}$$

According to (4-1) and (4-2), V_{aof} can be rewritten as

$$V_{aof} = \sum_{m=0}^{\infty}\sum_{n=1}^{\infty} A_{mn}\cos[(m\omega_{\text{inv}} \pm n\omega_0)t] \tag{4-3}$$

Equation (4-3) can be used as the reference voltage for H-Bridge modulation. Assuming modulation index of H-Bridge m_{a_h}=1, the minimum value of DC link voltage V_{cap} can be determined by

$$V_{cap} = \frac{1}{m_{a\_h}}\max_{t=0}^{\infty}(\sum_{m=0}^{\infty}\sum_{n=1}^{\infty} A_{mn}\cos[(m\omega_{\text{inv}} \pm n\omega_0)t]) = \sqrt{\frac{1}{3}}V_{dc} \tag{4-4}$$

According to (4-4), AOF DC link voltage V_{cap} is lower than main inverter DC link voltage V_{dc}, which proves the VA rating of AOF switch is lower than the main inverter switch as stated in Section 3.

The switching function for H-bridge can be derived from (4-3).

$$S_{aof} = \frac{\sum_{m=0}^{\infty}\sum_{n=0}^{\infty} A_{mn}\cos[(m\omega_{\text{inv}} + n\omega_0)t]}{V_{cap}} \tag{4-5}$$

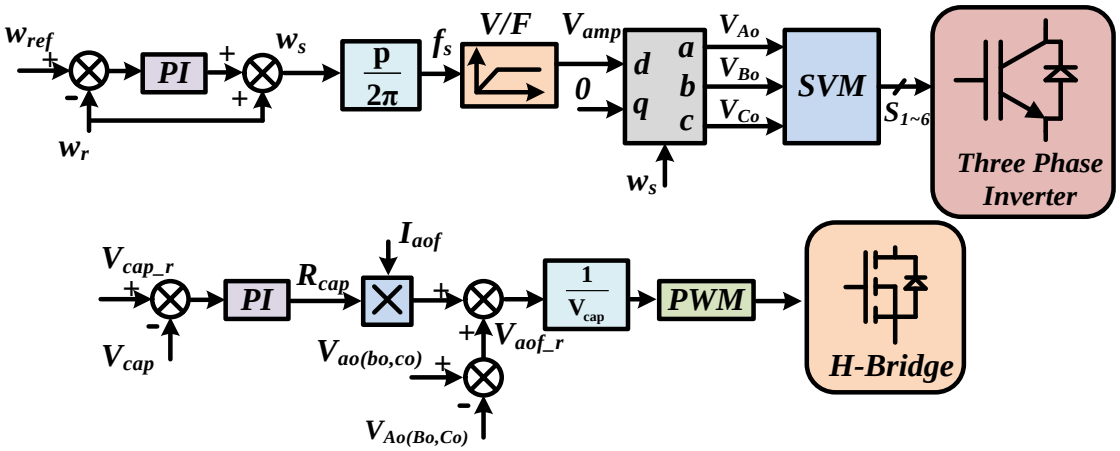

Fig. 4-2. Control strategy for three-phase ASD with AOF.

The overall control strategy is illustrated in Fig. 4-2. Voltage/Hertz speed control is implemented for induction motor speed adjustment [32]. The dq-abc transformation shown in Fig. 4-2 is determined by

$$\begin{bmatrix} V_{Ao} \\ V_{Bo} \\ V_{Co} \end{bmatrix} = \begin{bmatrix} \cos\omega_s t & -\sin\omega_s t & 1 \\ \cos(\omega_s t - \frac{2\pi}{3}) & -\sin(\omega_s t - \frac{2\pi}{3}) & 1 \\ \cos(\omega_s t + \frac{2\pi}{3}) & -\sin(\omega_s t + \frac{2\pi}{3}) & 1 \end{bmatrix} \bullet \begin{bmatrix} V_d \\ V_q \\ V_0 \end{bmatrix} \tag{4-6}$$

In order to generate the reference signal of AOF V_{aof_r}, $V_{ao(bo,co)}$ and $V_{Ao(Bo,Co)}$ should be achieved. $V_{Ao(Bo,Co)}$ is the low frequency sinusoidal signal (e.g 60Hz) which can be generated from digital controller. However, $V_{ao(bo,co)}$ shown in (4-2) is too complicated to be generated directly. Because main inverter switching function is

generated by digital controller itself, $V_{ao(bo,co)}$ can be generated by main inverter switching function indirectly.

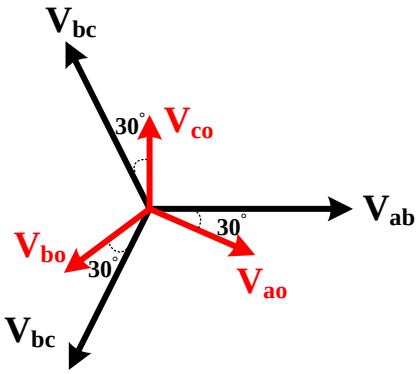

Fig. 4-3. Three-phase vector diagram.

The three-phase vector diagram is shown in Fig. 4-3. If S_1 – S_3 denote the switching function for phase A, B and C, respectively, the three-phase line-line voltage can be determined by

$$\begin{cases} V_{ab} = V_{dc}(S_1 - S_2) \\ V_{bc} = V_{dc}(S_2 - S_3) \\ V_{ca} = V_{dc}(S_3 - S_1) \end{cases} \tag{4-7}$$

According to Fig. 4-3, three-phase line-neural voltage can be expressed as

$$\begin{cases} V_{ao} = V_{dc}(\frac{2}{3}V_{ab} + \frac{1}{3}V_{bc}) \\ V_{bo} = V_{dc}(\frac{2}{3}V_{bc} + \frac{1}{3}V_{ca}) \\ V_{co} = V_{dc}(\frac{2}{3}V_{ca} + \frac{1}{3}V_{ab}) \end{cases} \tag{4-8}$$

Integrating (4-7) and (4-8), $V_{ao(bo,co)}$ can be achieved by main inverter switching function.

$$\begin{cases} V_{ao} = \frac{1}{3} V_{dc}(2S_1 - S_2 - S_3) \\ V_{bo} = \frac{1}{3} V_{dc}(2S_2 - S_1 - S_3) \\ V_{co} = \frac{1}{3} V_{dc}(2S_3 - S_1 - S_2) \end{cases} \quad (4\text{-}9)$$

4.2 Design Example

A 2/3 horsepower rated ASD system is designed to verify the operation principle of the proposed AOF. The specific operation specifications are shown in Table 4-1.

Table 4-1: Three-phase ASD system operation condition with AOF

Description	**Value**
Input line-line voltage V_{LL}	240V
Intermediate DC voltage V_{dc}	324V
Rated output power P_o	2/3hp
Main switching frequency f_{inv} AOF switching frequency f_s	2.1kHz 48kHz
DC link voltage V_{cap}	187V
Rated stator voltage $V_{AB(BC,CA)}$	230V
Rated frequency f_o	60Hz
Rated stator current $I_{A(B,C)}$	2.5A

For Output Filter L_a and C_a, the design criterion refers to single-phase ASD with AOF discussed in Section 3. As for DC link capacitor C_d, assuming no power loss in AOF, the DC link current is the product of switching function and AOF output current.

$$I_{cap}(t) = S_{aof} I_{aof}(t) \quad (4\text{-}10)$$

Due to AOF in series with the load, $I_{aof}(t)$ is equivalent to the load current.

$$I_{aof}(t) = \sqrt{2} I_{Ao(Bo,Co)} \cos(wt) \quad (4\text{-}11)$$

Integrating (4-5), (4-10) and (4-11), $I_{cap}(t)$ can be defined as

$$I_{cap}(t) = \frac{\sqrt{2}}{V_{cap}} \sum_{m=0}^{\infty} \sum_{n=1}^{\infty} A_{mn} \cos[(m\omega_{\text{inv}} \pm n\omega_0)t] I_{A(B,C)} \cos(wt) \tag{4-12}$$

Considering the positive half cycle of H-bridge $T_+ = DT_s$, the capacitor is charging by

$$\Delta Q = \int_{T_1}^{T_1 + D(t)T_s} I_{cap}(t)dt = C_d \Delta V_{cap} \tag{4-13}$$

Substituting (4-12) into (4-13), the minimum value of C_d can be defined as:

$$C_d \geq \frac{\sqrt{2} I_{A(B,C)} T_s}{\omega \Delta V_{cap\_\min}} \max[\sin(\omega T_1 + \omega T_s) - \sin \omega T_1] \tag{4-14}$$

Because switching cycle of H-bridge T_s is a very small interval compared to output current cycle, (4-14) can be rewritten as

$$C_d \geq \frac{\sqrt{2} I_{A(B,C)} T_s}{\omega \Delta V_{cap\_\min}} \max(\frac{d \sin(\omega t)}{d\omega}) \tag{4-15}$$

Due to $\frac{dsin(\omega t)}{dt} = \omega cos(\omega t)$, it is not difficult to find $\max\left(\frac{dsin(\omega t)}{dt}\right) = \omega$. Therefore, DC link capacitor C_d can be determined in accordance with the limit of DC link voltage ripple.

$$C_d \geq \frac{\sqrt{2} I_{A(B,C)} T_s}{\Delta V_{d\_\max}} \tag{4-16}$$

Based on the equations above and Table 4-1, the AOF parameters can be calculated as shown in Table 4-2.

To compare the value and volume between LC passive filter and AOF, the LC passive filter for three-phase ASD system is designed shown in Table 4-2, which refers to Section 3.2.

Table 4-2: Specifications of LC filter and AOF for three-phase ASD system

Description	**LC Filter**	**AOF**
Filter Capacitor C_a	15μF	10μF
Filter Inductor L_a	5.1mH	50μH
DC Link Capacitor C_d	N/A	200μF

The inductor and capacitor volume can be achieved by (3-26) and (3-29), respectively, which is detailed in Table 4-3.

Table 4-3: Volume comparison between LC filter and AOF in three-phase ASD

Description	**LC Filter**	**AOF**
Volume of C_a	3.5cm^3×3	2.1cm^3×3
Volume of L_a	533.9cm^3×3	5.2cm^3×3
Volume of C_{cap}	N/A	8.2cm^3×3
Volume of H-bridge and gate driver	N/A	35.1cm^3×3
Overall Volume	1612.2cm^3	151.8cm^3

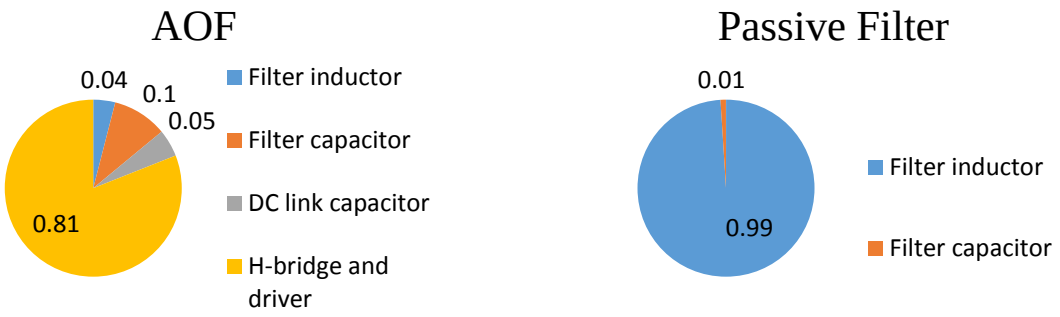

Fig. 4-4. Volume distribution.

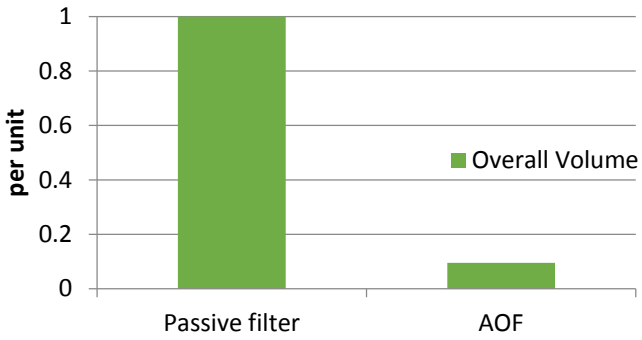

Fig. 4-5. Overall volume comparison.

Fig 4-5 shows the inductor accounts for most of the volume in the passive filter. As for AOF, H-bridge and gate driver occupy over 80%. Owing to the much smaller inductor employed in AOF, the overall volume of AOF reduces to about 10% of LC filter as shown Fig. 4-5. Note practical capacitor and inductor volume may be slightly different from the theoretic value.

According to (2-29) and Table 5.1 – 5.2, the three-phase AOF control-output transfer function can be expressed as:

$$G_{vd}(s) = \frac{\hat{v}_{aof}}{\hat{d}} = \frac{39s + 30680}{3\times10^{-11}s^3 + 2.36\times10^{-8}s^2 + 0.06s + 47.2} \tag{4-17}$$

The pole-zero plot is shown in Fig. 4-6. Because all of poles are located in the left half plane, it can achieve the stability. However, the stability margin is not enough due to p1 and p2 close to the imaginary axis.

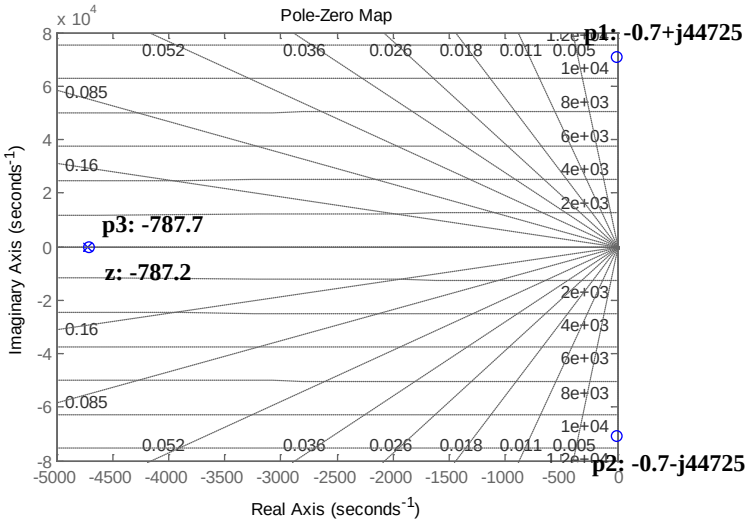

Fig. 4-6: Pole-zero map of three-phase AOF control-output transfer function.

4.3 Simulation Results

(1) Load step operation

The design example is simulated using PSIM. Fig. 4-7 illustrates the load transient operation. In Fig. 4-7(a), DC link voltage V_{cap} is nearly constant at 187V ($\frac{1}{\sqrt{3}}V_{dc}$). In addition, amplitude and frequency of AOF output voltage V_{aof} varies with the load transition. In Fig. 4-7(b), three phase stator voltages change from 230V/60Hz to 153V/40Hz, which demonstrates the constant V/Hz operation.

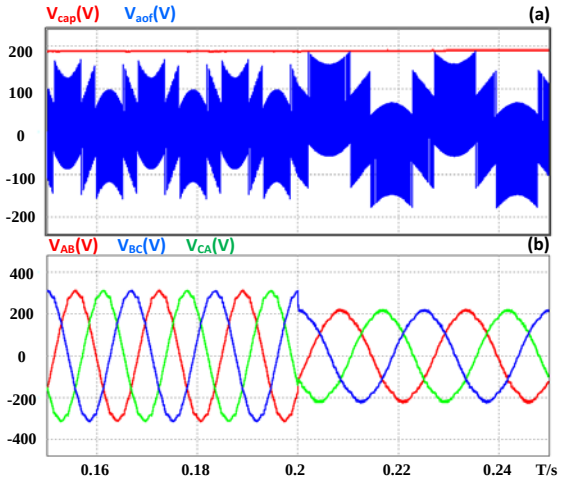

Fig. 4-7. Three-phase ASD with AOF load step operation. (a) AOF DC link voltage and output voltage. (b) Three-phase stator voltages.

(2) Line step operation

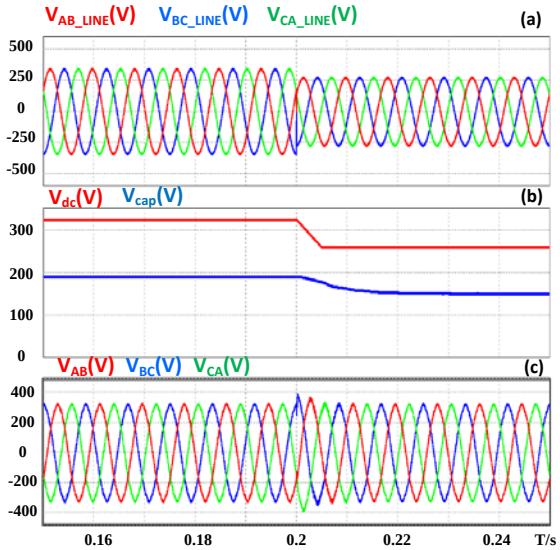

Fig. 4-8. Three-phase ASD with AOF line step operation. (a) Three-phase line-line voltage. (b) Intermediate DC link voltage and AOF DC link voltage. (c) Three-phase stator voltages.

The line step operation for three-phase ASD with AOF is illustrated in Fig. 4-8. In Fig. 4-8(a), the line-line voltage transfers from 240V to 190V at 0.2s. During this

transition, the DC link voltage of AOF changes from 187V to 150V with the intermediate DC voltage step-down shown in Fig. 4-8(b). It proves the ratio of DC link voltage and intermediate DC voltage still keeps $\frac{1}{\sqrt{3}}$. In Fig. 4-8(c), it can be observed that stator voltage keeps constant when line voltage sags.

(4) Harmonics comparison between LC filter and AOF

To verify the AOF advantage of harmonic elimination, the stator current harmonics comparison between LC filter and AOF is shown in Fig. 4-9. In the range of 20 ~ 20k Hz (audible frequency range), stator current harmonics in ASD with the proposed AOF are much lower than LC filter, especially around the 1st and 2nd switching frequency.

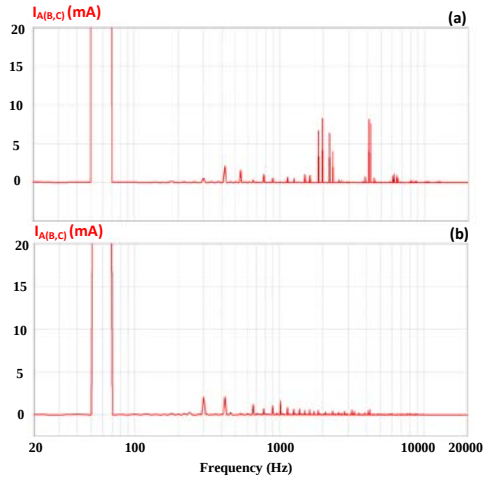

Fig. 4-9. FFT analysis of stator current harmonics operating at 230V/60Hz. (a) Three-phase ASD with LC filter. (b) Three-phase ASD with AOF.

4.4 Experimental Results

The 2/3 hp ASD system prototype is implemented and tested. The specifications of this prototype are the same as the design example shown in Table 4-1. The acoustic noise measurement system shown in Fig. 3-9 is used to analyze the acoustic noise spectra.

(1) 153V/40Hz operation condition

First, the prototype operating at 153V/40Hz is measured as shown in Fig. 4-10 ~ Fig. 4-13. Fig. 4-10 presents the main inverter output voltages which include abundant PWM harmonics. By using AOF, the three phase stator voltages only include the fundamental frequency voltage as shown in Fig. 4-11, and hence, there is no voltage overshoot in the motor terminal. In the same figure, the DC link voltage V_{cap} keeps constant at about $\frac{1}{\sqrt{3}}V_{dc}$, which is in accordance with the theory analysis. Fig. 4-10 and Fig. 4-11 verify the AOF effectively eliminate the switching frequency harmonics from the PWM mode inverter.

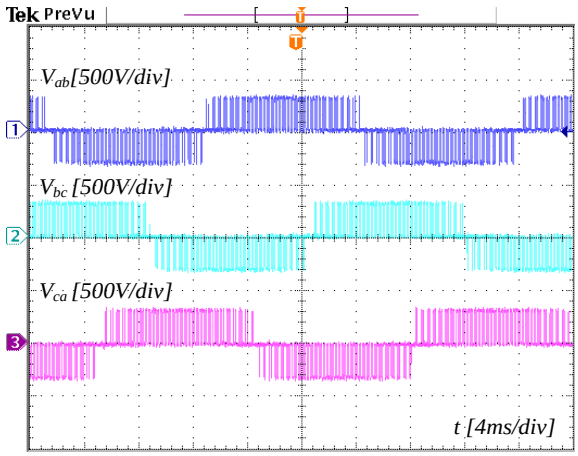

Fig. 4-10. Main inverter output voltage of three-phase ASD with AOF at 153V/40Hz condition.

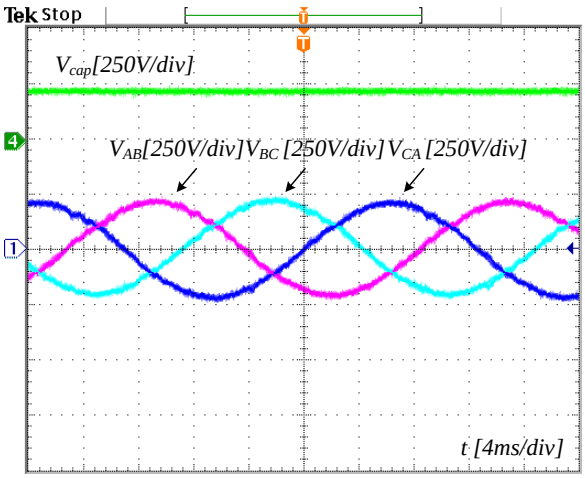

Fig. 4-11. DC link voltage and three phase stator voltage of three-phase ASD with AOF at 153V/40Hz condition.

Fig. 4-12 illustrates the stator currents harmonics comparison among no filter, LC filter and AOF. It can be observed that current harmonics are much lower by using AOF, especially for harmonics around low switching frequency sidebands.

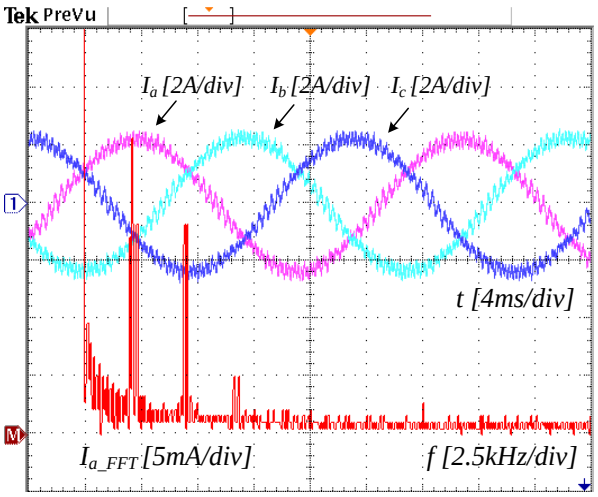

(a)

Fig. 4-12. Three phase stator current and frequency spectrum of three-phase ASD at 153V/40Hz condition. (a) without filter. (b) with LC passive filter. (c) with AOF.

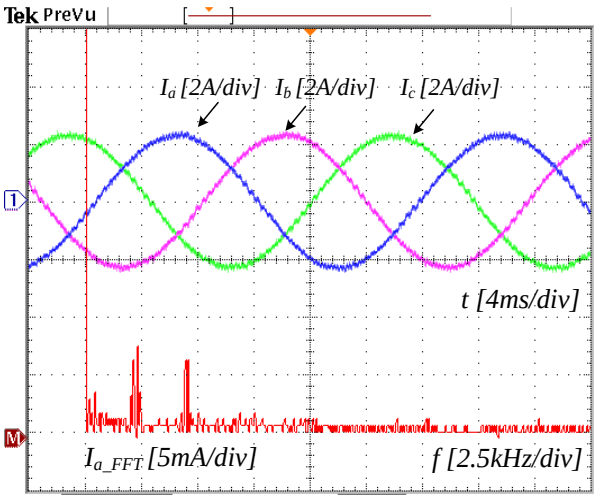

(b)

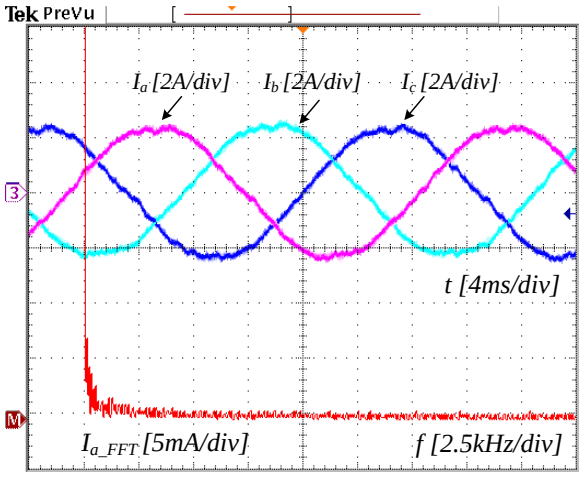

(c)

Fig. 4-12. Continued

Fig. 4-13 demonstrates the acoustic noise spectrum comparison among no filter, LC filter and AOF. In Fig. 4-13(b), acoustic noise is reduced by using LC filter, however, some noise spikes are still distributed around 1st and 2nd order switching frequency. It proves the analysis in Section 2 that current harmonics in low switching frequency cause the corresponding acoustic noise peaking. Last, these noise spikes are dramatically

suppressed by using AOF as shown in Fig. 4-13(c). In this case, the dominant area of acoustic noise is only arranged in the fundamental frequency.

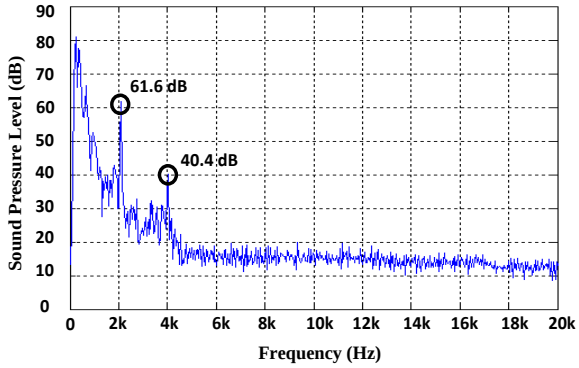

(a)

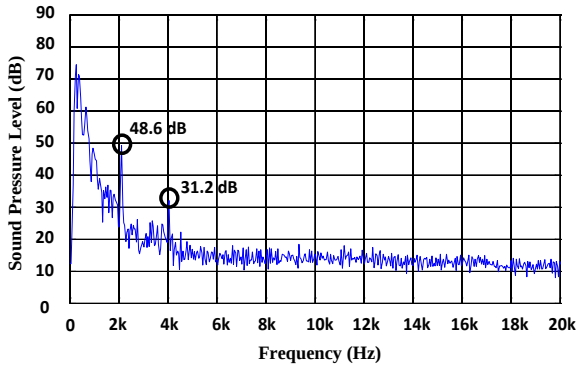

(b)

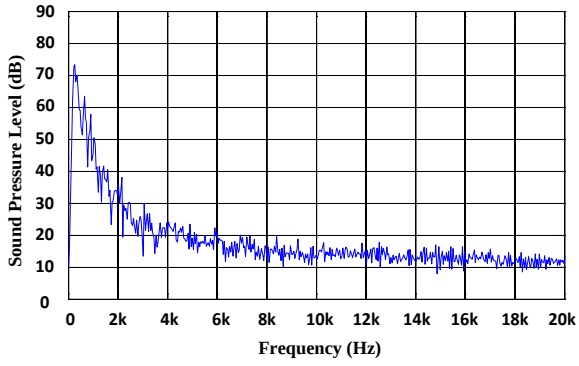

(c)

Fig. 4-13. Acoustic noise spectrum of three-phase ASD system at 153V/40Hz condition. (a) without filter. (b) with LC passive filter. (c) with AOF.

(2) 230V/60Hz operation condition

The 230V/60Hz operation condition (rated condition) is also measured as shown in Fig. 4-14 ~ Fig. 4-17. Fig. 4-14 and Fig. 4-15 illustrate AOF removes most of harmonics from PWM mode inverter and provides the almost sinusoidal waveforms at the motor terminal. In addition, DC link voltage in 230V/60Hz condition (Fig. 4-11) equals to 153V/40Hz condition (Fig. 4-15) due to invariant intermediate DC voltage V_{dc}.

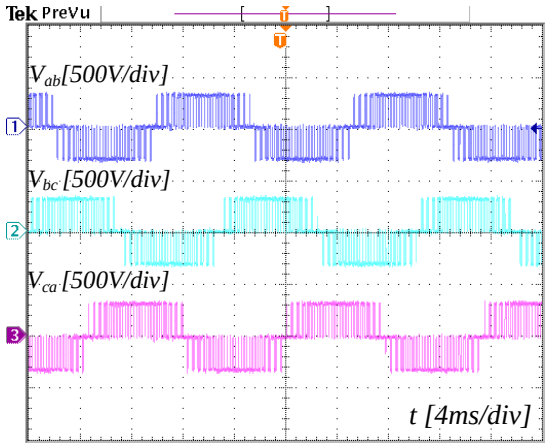

Fig. 4-14. Main inverter output voltage of three-phase ASD with AOF at 230V/60Hz condition.

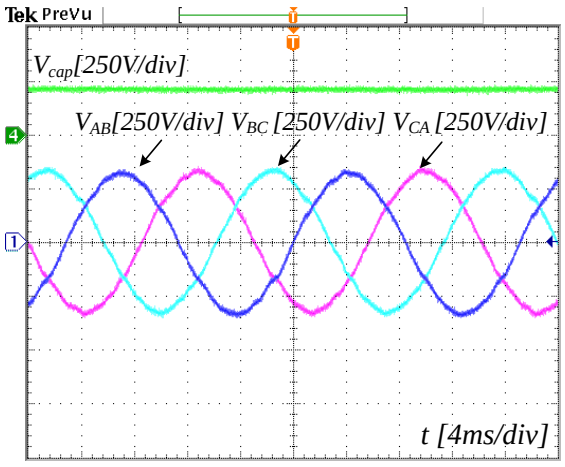

Fig. 4-15. DC link voltage and three phase stator voltage of three-phase ASD with AOF at 230V/60Hz condition.

Fig. 4-16 shows the stator current harmonics comparison among no filter, passive filter and AOF. Even though passive filter is beneficial to reduce the current harmonics, some harmonics are still distributed in 1st and 2nd order switching frequency sidebands shown in Fig 5-16(b). In similar with 153V/40Hz condition, AOF operating at 230V/60Hz can also efficiently eliminate the stator current harmonics in low witching frequency sidebands as shown in Fig. 4-16(c).

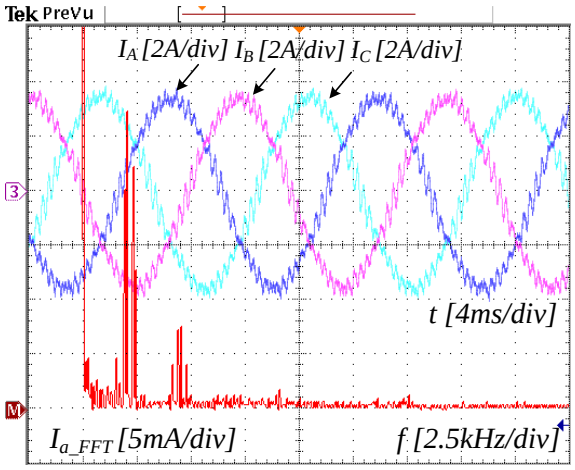

(a)

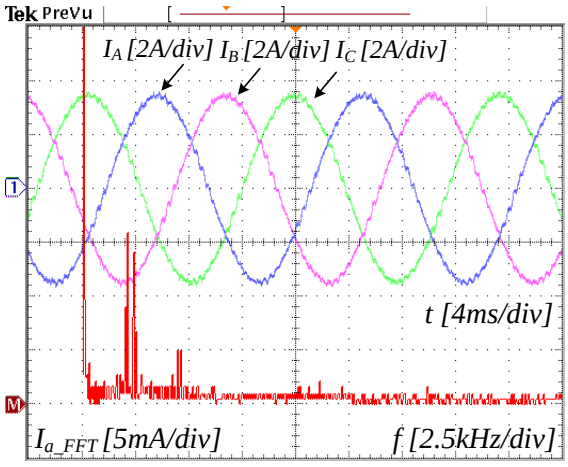

(b)

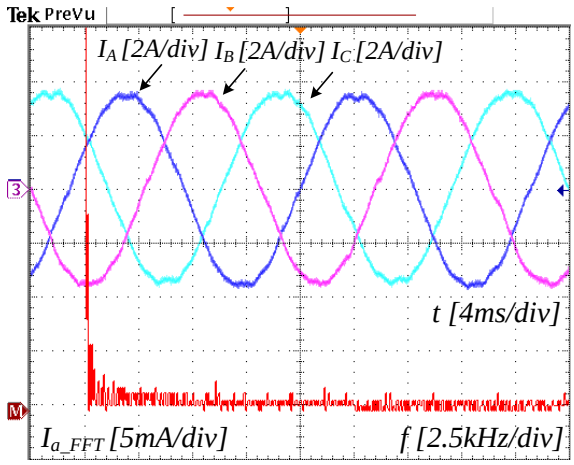

(c)

Fig. 4-16. Three phase stator current and frequency spectrum of three-phase ASD at 230V/60Hz condition. (a) without filter. (b)with passive LC filter. (c) with AOF.

Corresponding to stator current harmonics spectrum shown in Fig. 4-16(a), huge noise spikes occur at 1st and 2rd order switching frequency sidebands, which is presented in Fig. 4-17(a). By using passive filter, these noise spikes are reduced to 52.1 dB and 30.9 dB as shown in Fig. 4-17(b). In similar with 153V/40Hz condition, there is no noise spike due to AOF at 230V/60Hz condition shown in Fig. 4-17(c).

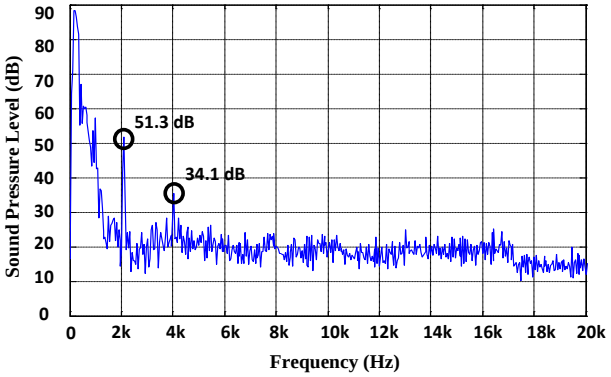

(a)

Fig. 4-17. Acoustic noise spectrum of three-phase ASD system at 230V/60Hz condition. (a) without filter. (b) with LC passive filter. (c) with AOF.

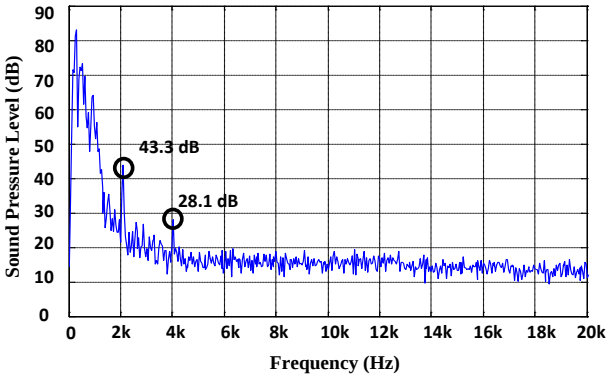

(b)

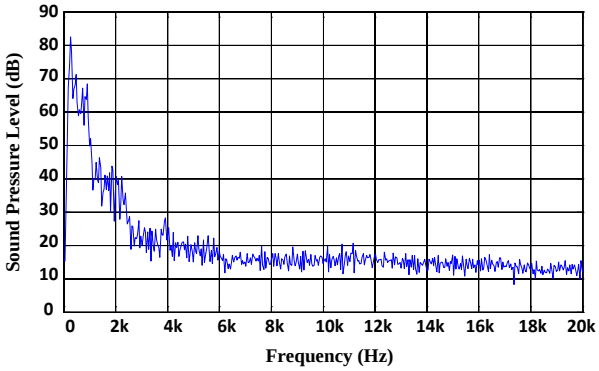

(c)

Fig. 4-17 Continued.

The overall acoustic noise of three-phase ASD system is presented in Fig. 4-18. Acoustic noise is the lowest at different operation conditions by using AOF.

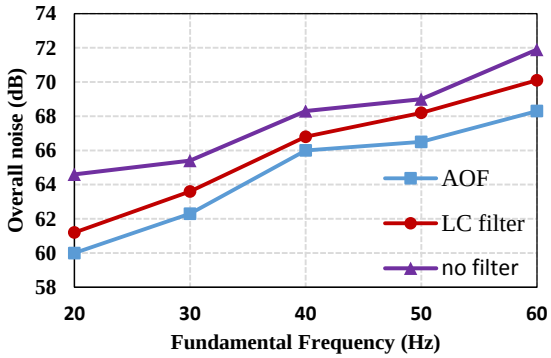

Fig. 4-18. Overall noise emitted by three-phase ASD at various fundamental frequencies operation conditions.

4.5 Conclusion

In this Section, the proposed AOF is used in three-phase ASD system. The system configuration and control strategy including AOF and three-phase ASD are discussed. The 2/3 hp design example proves the proposed AOF occupies much smaller area than the traditional passive filter. The advantage of AOF in the acoustic noise reduction is validated by the simulation and experiment.

5. CONCLUSION AND FUTURE WORK

In this thesis, the design of the active output filter (AOF) is introduced. The proposed AOF is implemented by an H-bridge and a DC link capacitor. The control strategy for the H-bridge maintains the DC link voltage and realizes the harmonics injection.

The proposed AOF can replace the bulky LC passive filter in single-phase ASD and three-phase ASD. The design example for 1/2 hp single-phase ASD system proves the AOF volume is only 6.5% of the passive filter. In addition, 2/3 hp three-phase ASD system is presented to demonstrate power density of AOF is about 10 times higher than LC filter.

Simulation results show the dynamic operation of ASD with AOF. Experimental results show that the stator voltages at motor terminals are approximately sinusoidal waveforms without voltage spikes by using AOF. Even though traditional LC filter can eliminate high switching frequency harmonics, low switching frequency harmonics such as 1^{st} and 2^{nd} order harmonics still exist in ASD system. In the ASD with AOF, harmonics in the whole spectrum are suppressed, and hence, the acoustic noise is reduced accordingly, especially for low switching frequency acoustic noise.

Future work will be done to explore the following areas:

- More experiments for transient operation of single-phase ASD and three-phase ASD.
- Applying AOF for open-end winding ASD system
- Electro-magnetic analysis of induction motor based on Maxwell

- H-bridge and gate driver volume optimization

REFERENCES

[1] International Energy Agency, Energy-efficiency policy opportunities for electric motor-driven systems, 2011. url: www.iea.org/publications/freepublications/publication/EE__for_ElectricSystems.pdf

[2] U.S Energy Information Administration , Electric Power Annual Report, 2014. url: http://www.eia.gov/electricity/annual/

[3] U.S. Energy Information Administration, International Energy Outlook, 2013. url: http://www.eia.gov/forecasts/ieo/pdf/0484(2013).pdf

[4] K. Lee, T. M. Jahns, W. E. Berkopec and T. A. Lipo, "Closed-form analysis of adjustable-speed drive performance under input-voltage unbalance and sag conditions," in *IEEE Transactions on Industry Applications*, vol. 42, no. 3, pp. 733-741, May-June 2006.

[5] Ned Mohan, and Tore M Undeland (2003). Power electronics: converters, applications, and design. John Wiley & Sons, Hoboken, NJ.

[6] Hwang, Sangmoon (1994). "Analysis of vibration and acoustic noise in permanent magnet motors." PhD thesis, University of California, Berkeley, Berkeley, CA.

[7] Gieras, Jacek F., Chong Wang, and Joseph Cho Lai (2005). Noise of polyphase electric motors. CRC press, Boca Raton, FL.

[8] Kenjo, Takashi, and Shigenobu Nagamori (1985). Permanent-magnet and brushless DC motors. Oxford University Press, New York, NY.

[9] Xu, M., and R. D. Marangoni. "Vibration analysis of a motor-flexible coupling-rotor system subject to misalignment and unbalance, Part I: theoretical model and analysis." *Journal of Sound and Vibration*, 176.5 (1994): 663-679.

[10] Finley, William R., Mark M. Hodowanec, and Warren G. Holter. "An analytical approach to solving motor vibration problems." Petroleum and Chemical Industry Conference, 1999. *Industry Applications Society 46th Annual*. IEEE, 1999.

[11] A. Ruiz-Gonzalez, M. J. Meco-Gutierrez, F. Perez-Hidalgo, F. Vargas-Merino and J. R. Heredia-Larrubia, "Reducing acoustic noise radiated by inverter-fed induction motors controlled by a new PWM strategy," *IEEE Trans. Ind. Electron.*, vol. 57, no. 1, pp. 228-236, 2010.

[12] H. Jordan. “Approximate calculation of the noise produced by motor,” ENG, 1949, (10): 22~26.

[13] R. S. Girgis and S. P. Vermas, "Method for accurate determination of resonant frequencies and vibration behaviour of stators of electrical machines," in *IEE Proceedings B - Electric Power Applications*, vol. 128, no. 1, pp. 1-, January 1981.

[14] Z. Q. Zhu and D. Howe, "Improved methods for prediction of electromagnetic noise radiated by electrical machines," in *IEE Proceedings - Electric Power Applications*, vol. 141, no. 2, pp. 109-120, Mar 1994.

[15] D. E. Cameron, J. H. Lang and S. D. Umans, "The origin and reduction of acoustic noise in doubly salient variable-reluctance motors," in *IEEE Transactions on Industry Applications*, vol. 28, no. 6, pp. 1250-1255, Nov/Dec 1992.

[16] A. C. Binojkumar, B. Saritha and G. Narayanan, "Acoustic noise characterization of space-vector modulated induction motor drives—an experimental approach," in *IEEE Transactions on Industrial Electronics*, vol. 62, no. 6, pp. 3362-3371, June 2015.

[17] C. Lin and B. Fahimi, "Prediction of acoustic noise in switched reluctance motor drives," in *IEEE Transactions on Energy Conversion*, vol. 29, no. 1, pp. 250-258, March 2014.

[18] S. Huang, M. Aydin and T. A. Lipo, "Electromagnetic vibration and noise assessment for surface mounted PM machines," *Power Engineering Society Summer Meeting, 2001*, Vancouver, BC, Canada, 2001, pp. 1417-1426 vol.3.

[19] J. Le Besnerais, V. Lanfranchi, M. Hecquet and P. Brochet, "Characterization and reduction of audible magnetic noise due to PWM supply in induction machines," in *IEEE Transactions on Industrial Electronics*, vol. 57, no. 4, pp. 1288-1295, April 2010.

[20] R. S. Colby, F. M. Mottier and T. J. E. Miller, "Vibration modes and acoustic noise in a four-phase switched reluctance motor," in *IEEE Transactions on Industry Applications*, vol. 32, no. 6, pp. 1357-1364, Nov/Dec 1996.

[21] Danfoss (2005). “Output filter design guide”. url: http://files.danfoss.com/documents/PE/doc_MG90N202.pdf

[22] M. M. Bech, F. Blaabjerg and J. K. Pedersen, "Random modulation techniques with fixed switching frequency for three-phase power converters," *Power Electronics Specialists Conference, 1999. PESC 99. 30th Annual IEEE*, Charleston, SC, 1999, pp. 544-551 vol.1.

[23] T. G. Habetler and D. M. Divan, "Acoustic noise reduction in sinusoidal PWM drives using a randomly modulated carrier," in *IEEE Transactions on Power Electronics*, vol. 6, no. 3, pp. 356-363, Jul 1991.

[24] Y. C. Lim, S. O. Wi, J. N. Kim and Y. G. Jung, "A pseudorandom carrier modulation scheme," in *IEEE Transactions on Power Electronics*, vol. 25, no. 4, pp. 797-805, April 2010.

[25] F. Z. Peng. "Harmonic sources and filtering approaches." *IEEE Mag. Ind. Applicat.*, vol.7, no.4, pp.18-25, 2001.

[26] W. C. Lo, C. C. Chan, Z. Q. Zhu, Lie Xu, D. Howe and K. T. Chau, "Acoustic noise radiated by PWM-controllel induction machine drives," *IEEE Trans. Ind. Electron.*, vol. 47, no. 4, pp. 880-889, 2000.

[27] A. Ruiz-Gonzalez, F. Vargas-Merino, F. Perez-Hidalgo, M. J. Meco-Gutierrez and J. R. Heredia-Larrubia, "Low switching PWM strategy to reduce acoustic noise radiated by inverter-fed induction motors," *2010 IEEE International Symposium on Industrial Electronics*, Bari, 2010, pp. 1353-1358.

[28] H. Tischmacher, I. P. Tsoumas, B. Eichinger and U. Werner, "Case studies of acoustic noise emission from inverter-fed asynchronous machines," *IEEE Trans. Ind. Applicat.*, vol. 47, no. 5, pp. 2013-2022, Sept.-Oct. 2011.

[29] McLyman, Colonel Wm T (2011). Transformer and inductor design handbook. CRC press, Boca Raton, FL.

[30] D. G. Holmes, Thomas A. Lipo (2003). “Pulse width modulation for power converters: principles and practice.” John Wiley & Sons, Hoboken, NJ.

[31] M. Huang, F. Blaabjerg, Y. Yang and W. Wu, "Step by step design of a high order power filter for three-phase three-wire grid-connected inverter in renewable energy system," *in Proc. Power Electronics for Distributed Generation Systems (PEDG), 4th IEEE International Symposium on*, pp. 1-8. 2013.

[32] A. Munoz-Garci, T. A. Lipo, and D. W. Novotny. “A new induction motor V/f control method capable of high-performance regulation at low speeds.” *IEEE Trans. Applicat.*, vol. 34, no. 4, pp. 813-821, 1998.

[33] K. Iwaya, T. Noguchi, "High-frequency switched mode power with small capacity filter inverters." *in Porc. Industrial Electronics Society Annual Conference (IECON)*, 2004, pp.35-40.

[34] W. K. Henson *et al*., "Estimating oxide thickness of tunnel oxides down to 1.4 nm using conventional capacitance-voltage measurements on MOS capacitors," *IEEE Electron. Device Letters*, vol. 20, no. 4, pp. 179-181, 1999.